Published for SISSA by Springer

Received: *February 6, 2024*
Accepted: *March 23, 2024*
Published: *April 24, 2024*

Dark Radiation Constraints on Heavy QCD Axions

David I. Dunsky[a,b] **Lawrence J. Hall**[a,b] **and Keisuke Harigaya**[c]

[a]*Department of Physics, University of California, Berkeley, California 94720, U.S.A.*
[b]*Theoretical Physics Group, Lawrence Berkeley National Laboratory, Berkeley, California 94720, U.S.A.*
[c]*Theoretical Physics Department, CERN, Geneva, Switzerland*

E-mail: ddunsky@berkeley.edu, ljhall@lbl.gov, kharigaya@uchicago.edu

Abstract: The naturalness problem of PQ symmetry motivates study of the heavy QCD axion, with masses $m_a > 1\,\mathrm{MeV}$ generated at scales above the QCD scale, and low values of the PQ symmetry breaking scale, f_a. We compute the abundance of such axions in a model-independent way, assuming only that they freeze-out after reheating from inflation, and are not subsequently diluted by new physics. If these axions decay between neutrino decoupling and the last scatter era of the Cosmic Microwave Background (CMB), they dilute the neutrinos and their abundance is constrained by CMB measurements of the energy density in dark radiation, N_{eff}. We accurately compute this bound using a numerical code to evolve the axion momentum distribution, including many key processes and effects previously ignored. We assume that the only relevant axion decays are to final states involving Standard Model particles. We determine regions of (m_a, f_a) that will give a signal in N_{eff} at CMB Stage 4 experiments. We similarly compute the N_{eff} bound and CMB Stage 4 signal for heavy axions that can decay to light mirror photons. Finally, we compute the bounds on heavy axions with mass below 1 MeV that decay after the era of CMB last scatter, from their contribution to cold or hot dark matter or N_{eff} at this era.

Keywords: Axions and ALPs, Cosmology of Theories BSM

ArXiv ePrint: 2205.11540

Open Access, © The Authors.
Article funded by SCOAP[3].

https://doi.org/10.1007/JHEP04(2024)130

JHEP04(2024)130

Contents

1 Introduction

The smallest dimensionless parameter of the Standard Model is the strong CP parameter $\bar{\theta} \lesssim 10^{-10}$. This small parameter can be understood as resulting from a discrete spacetime symmetry, CP [1, 2] or P [3–5], or from a global Abelian Peccei-Quinn (PQ) symmetry [6, 7]. Imposing a PQ symmetry appears odd, as the symmetry is necessarily broken by the QCD anomaly; but it may appear as an approximate accidental symmetry at low energies [8]. In such scenarios, the PQ symmetry is expected to be explicitly broken by higher-dimensional operators, typically preventing sufficient dynamical relaxation of $\bar{\theta}$ towards zero even if they are suppressed by powers of the Planck mass, $M_{\rm Pl}$.

For example, if ϕ is the field that spontaneously breaks the PQ symmetry at scale f_a, in standard axion theories the interactions $\lambda_n \phi^{n+4}/M_{\rm Pl}^n$ must be suppressed to solve the strong CP problem,

$$\lambda_n \;<\; 10^{(-46+10n)} \left(\frac{10^8\,\text{GeV}}{f_a}\right)^{4+n} . \tag{1.1}$$

Even for the lowest values of f_a allowed by observations, of order $10^8\,$GeV, operators of dimension 5 through 8 are highly constrained; and the problem gets worse rapidly as f_a is increased. It is non-trivial to find theories where an accidental symmetry is protected to such high order, typically requiring significant additions to the theory. Even if one simply imposes

JHEP04(2024)130

the PQ symmetry as a classical symmetry, it may be broken by quantum gravity [9, 10], reintroducing the quality problem [11–14]. Since the PQ symmetry must have a QCD anomaly, this PQ quality problem cannot be avoided by promoting it to a gauge symmetry. On the other hand, P and CP can be embedded in higher-dimensional gauge symmetries [15, 16] making them attractive avenues for the strong CP problem.

The severity of this PQ quality problem, shown in (1.1), applies to the standard QCD axion, where its mass arises from non-perturbative QCD physics at the Fermi scale. It motivates theories with a heavy QCD axion, where the axion mass arises from physics at higher energy scales and is much larger. While the conventional QCD axion mass is less than the eV scale, these theories allow the axion mass to be larger than the MeV scale, removing constraints from stellar cooling and/or beam-dump experiments and allowing greatly reduced symmetry breaking scales. Removing dimension 5 or lower operators by a gauge symmetry,[1] which may underlie the accidental PQ symmetry, the shift of $\bar{\theta}$ from zero by a dimension 6 operator is sufficiently small if

$$m_a \gtrsim \text{MeV} \left(\frac{f_a}{3 \times 10^4 \,\text{GeV}} \right)^2 . \tag{1.2}$$

In heavy axion theories there is a limit to how heavy the axion can be, and solving the quality problem then motivates low values of f_a.

For f_a of order $(10^4\text{–}10^7)$ GeV, a strong cosmological limit on the heavy QCD axion arises for masses in the (MeV–GeV) range. Such axions may decay after neutrino decoupling, diluting the neutrino abundance, as found for axion-like particles in [18]. There is a powerful bound on this dark radiation from measurements of the Cosmic Microwave Background radiation (CMB) by the Planck Collaboration [19], $N_{\text{eff}} = 2.96^{+0.34}_{-0.33}$ at 95% c.l., and a significantly more accurate determination, with uncertainties smaller by almost an order of magnitude, is a key objective of CMB Stage 4 experiments [20]. In this paper we study this bound on (m_a, f_a) in a model-independent way, including many effects previously ignored, several arising from axion-meson interactions. See refs. [21–28] for studies on axions that are light and stable and directly contribute to dark radiation, and ref. [29–31] for axions as hot dark matter.

There is a long history of theories with a heavy QCD axion, motivated by both the quality problem and the interest in reducing f_a so that the axion is more visible. One simple possibility is that QCD, or part of the gauge group in which it is embedded, becomes strong in the UV, so that there is an important contribution to the axion potential from short distance instantons [32–37]. It is important that these instantons do not probe new CP violating phases, so that the new contribution to the potential aligns $\bar{\theta}$ to be sufficiently small. The growth in the QCD coupling in the UV could also arise from extra spatial dimensions [38].

Another simple way to make the QCD axion heavy is to introduce a Z_2 symmetry that transforms the Standard Model (SM) into a mirror sector. The Z_2 symmetry is spontaneously or softly broken so that the mirror electroweak scale is much larger than the SM weak scale, $v' \gg v$. The mirror quarks are then much heavier than the SM quarks, so that below the mirror quark masses the QCD$'$ coupling runs faster than the QCD coupling and confines at

[1] In models where the spontaneous PQ breaking occurs by hidden quark condensation [17], this only requires the removal of hidden quark mass terms.

JHEP04(2024)130

a scale much above the QCD scale, $\Lambda' \gg \Lambda$. When introducing a PQ field that is Z_2 even, the resulting axion couples with the same strength to SM and mirror gluons, and hence its mass is larger than the conventional QCD axion by a factor of roughly $(\Lambda'/\Lambda)^2$. The first implementations of this idea [39, 40] used a Weinberg-Wilczek axion [41, 42], with the PQ symmetry spontaneously broken by Higgs vevs. In this case the axion decay constant f_a is large, of order v', and while these theories ameliorate the quality problem of (1.1), (1.2), solving the problem requires contrived arrangements. On the other hand, in the theories considered in [43–45] using a KSVZ axion [46, 47], the heavy QCD axion mass is

$$m_a \sim 100\,\mathrm{MeV}\left(\frac{v'}{10^8\,\mathrm{GeV}}\right)^{8/11}\left(\frac{10^4\,\mathrm{GeV}}{f_a}\right) \tag{1.3}$$

so that the quality problem is solved by taking $f_a \ll v'$. As always, one still needs to understand PQ in operators of dimension ≤ 4 as an accidental consequence of gauge symmetries [8]. If the mirror photon in these theories is light, the CMB constraints from dark radiation are modified, which we also study.

The constraints from dark radiation on the axion mass and its couplings have been studied in the literature. Refs. [18, 48, 49] consider an axion-like particle that couples only to photons, and do not consider axion-gluon couplings. As we will see, the axion-gluon coupling, which leads to axion-meson couplings, helps to keep the axion in thermal equilibrium, so that the Boltzmann suppression of the axion abundance is more effective, relaxing the constraint on (m_a, f_a). Ref. [43] studies the mirror QCD case with an axion-mirror photon coupling but, while the decay of the axion into three pions is taken into account, axion-pion scattering and other axion-meson interactions are not included.

This paper is organized as follows. Section 2 shows the Lagrangian of the theory above and below the QCD scale. Section 3 describes the computation of the dark radiation abundance with a set of Boltzmann equations and shows the resultant N_{eff}. Section 4 discusses the case with a mirror photon. Section 5 shows a complementary constraint from dark matter overproduction for a sufficiently light axion that decays after the matter-radiation equality, where the N_{eff} constraint is not applicable. We conclude the paper with section 6.

2 The effective theory above and below the QCD scale

In this paper, we study a heavy axion with interactions above the QCD scale given by

$$\mathcal{L} = \frac{1}{2}\partial^\mu a \partial_\mu a - \frac{1}{2}m_a^2 a^2 + \frac{g_3^2}{32\pi^2}\frac{a}{f_a}G_{\mu\nu}\tilde{G}^{\mu\nu} + \frac{e^2}{32\pi^2}\frac{E}{N}\frac{a}{f_a}F_{\mu\nu}\tilde{F}^{\mu\nu}. \tag{2.1}$$

We assume that the axion couplings with up, down, and electron axial currents are negligible. E/N is the ratio of the electromagnetic and QCD anomalies of the PQ symmetry. For a KSVZ axion with electrically neutral heavy quarks, $E/N = 0$. For complete representations of SU(5), $E/N = 8/3$.

In models with a large axion mass from mirror QCD, the axion may also couple to mirror photons. We include the effect of mirror photons on N_{eff} in section 4. Note that mirror-photon effects are negligible if the PQ symmetry does not have an electromagnetic

JHEP04(2024)130

anomaly and the mirror quarks are much heavier than the mirror QCD scale, which causes the mixing between the axion and mirror mesons composed of mirror quarks to be small. The analysis of section 2 and 3 is also applicable to the case where the mirror photon is massive and decouples by the QCD phase transition.

After an axial rotation to remove the coupling of the axions to gluons, below the QCD scale, the interactions of the axion with mesons and photons are described by the chiral Lagrangian, which, to leading order in p^2, is

$$\mathcal{L}_{\text{chiral}} = \frac{f_\pi^2}{4}\text{Tr}\{D^\mu U^\dagger D_\mu U\} + \frac{f_\pi^2}{4}\text{Tr}\{2BM_q U + \text{h.c.}\} + \frac{1}{2}\frac{\partial^\mu a}{f_a}\text{Tr}\{Q_A\lambda^a\}J_\mu^a + \frac{e^2}{32\pi^2}\left(\frac{E}{N} - \frac{8}{3}Q_u - \frac{2}{3}Q_d - \frac{2}{3}Q_s\right)\frac{a}{f_a}F_{\mu\nu}\tilde{F}^{\mu\nu}, \tag{2.2}$$

where $f_\pi = 93\,\text{MeV}$, B is a strong interaction parameter of order the QCD scale, J_μ^a is the SU(3) axial current given by

$$J_\mu^a = \frac{i}{4}f_\pi^2\text{Tr}\{\lambda^a(UD^\mu U^\dagger - U^\dagger D^\mu U)\}, \tag{2.3}$$

and

$$Q_A = \begin{pmatrix} Q_u & & \\ & Q_d & \\ & & Q_s \end{pmatrix} \tag{2.4}$$

is the quark charge matrix for the transformation that eliminates the axion-gluon coupling with $\text{Tr}\ Q_A = 1$.

The meson nonet and quark mass matrices are given by

$$U = \exp i\frac{\sqrt{2}}{f_\pi}\begin{pmatrix} \frac{\pi_0}{\sqrt{2}} + \frac{\eta_8}{\sqrt{6}} + \frac{\eta_0}{\sqrt{3}} & \pi^+ & K^+ \\ \pi^- & -\frac{\pi_0}{\sqrt{2}} + \frac{\eta_8}{\sqrt{6}} + \frac{\eta_0}{\sqrt{3}} & K^0 \\ K^- & \bar{K}^0 & -2\frac{\eta_8}{\sqrt{6}} + \frac{\eta_0}{\sqrt{3}} \end{pmatrix}, \tag{2.5}$$

$$M_q = \begin{pmatrix} m_u e^{i\frac{a}{f_a}Q_u} & & \\ & m_d e^{i\frac{a}{f_a}Q_d} & \\ & & m_s e^{i\frac{a}{f_a}Q_s} \end{pmatrix}. \tag{2.6}$$

When calculating the effect of axion-meson scattering at energies below $\Lambda_{\text{QCD}} \approx 150\,\text{MeV}$, we limit ourselves to the relevant two-dimensional subspace, $\text{SU}(2)_L \times \text{SU}(2)_R \to \text{SU}(2)_V$, since the only active QCD degrees of freedom are pions. For axion masses above Λ_{QCD}, the chiral perturbation based on the symmetry $\text{SU}(2)_L \times \text{SU}(2)_R \to \text{SU}(2)_V$ breaks down. In this case, the axion may decay to heavy mesons like η and K, or for sufficiently large m_a, directly to gluons. Consequently, we use the results of [50] for the axion decay rate into mesons, gluons, and photons (including the enhancement in the axion-photon coupling from $a - \eta(\eta')$ mixing) for $m_a > m_\pi$. We discuss this further in the following section, but for now focus on the $\text{SU}(2)_V$ subspace which is sufficient for inferring axion-meson scattering in the early Universe.

In this two-dimensional subspace, we take the Q matrix proportional to the identity in isospin space with $Q_u = Q_d = 1/2$, so that kinetic mixing between the axion and pion is

JHEP04(2024)130

absent, though mass mixing is present. Expanding out the chiral Lagrangian (2.2) generates the following axion-pion mass matrix and interactions

$$\begin{aligned}\mathcal{L}_{a,\pi} = &-\frac{1}{2}\begin{pmatrix}\pi_0 & a\end{pmatrix}\begin{pmatrix}B(m_u+m_d) & B(f_\pi/f_a)\,(Q_u m_u - Q_d m_d)\\ B(f_\pi/f_a)\,(Q_u m_u - Q_d m_d) & m_a^2 + B(f_\pi/f_a)^2\,(Q_u^2 m_u + Q_d^2 m_d)\end{pmatrix}\begin{pmatrix}\pi_0\\ a\end{pmatrix}\\ &+\frac{B(Q_u m_u + Q_d m_d)}{24 f_\pi^2}(\pi_0^4 + 4\pi_-\pi_+\pi_0^2) + \frac{B(Q_u m_u - Q_d m_d)}{6 f_\pi}\frac{a}{f_a}(\pi_0^3 + 2\pi_0\pi_+\pi_-)\\ &+\frac{1}{3 f_\pi^2}(\pi_+\pi_0\,\partial^\mu\pi_-\partial_\mu\pi_0 + \pi_-\pi_0\,\partial^\mu\pi_+\partial_\mu\pi_0 - \pi_0^2\,\partial^\mu\pi_-\partial_\mu\pi_+ - \pi_-\pi_+\,\partial^\mu\pi_0\partial_\mu\pi_0). \quad (2.7)\end{aligned}$$

From the $\pi_0 - a$ mass matrix in the limit $f_a \gg f_\pi$, we can identify $B = m_\pi^2/(m_u + m_d)$. Moreover, since we study axions heavier than the standard QCD axion, $m_a f_a \gg m_\pi f_\pi$, and we can thus drop the second term in the bottom right entry of the mass matrix.

The $\pi_0 - a$ mass matrix is diagonalized by the rotation

$$\begin{pmatrix}\pi_0\\ a\end{pmatrix} = \begin{pmatrix}\cos\theta & \sin\theta\\ -\sin\theta & \cos\theta\end{pmatrix}\begin{pmatrix}\hat{\pi}_0\\ \hat{a}\end{pmatrix} \quad (2.8)$$

with

$$\tan 2\theta = \frac{f_\pi}{f_a}\frac{1-z}{1+z}\frac{1}{1-r^2}, \quad (2.9)$$

where $r \equiv m_a/m_\pi$ and $z \equiv m_u/m_d \simeq 0.47$ [51]. In terms of the mass eigenstates $\hat{\pi}_0, \hat{a}$, the interaction of the axion with three pions is described by

$$\mathcal{L}_{\hat{a},\hat{\pi}} \supset \frac{A}{f_a f_\pi}\frac{1}{1-r^2}\left[\partial^\mu\hat{a}(\pi_-\hat{\pi}_0\,\partial_\mu\pi_+ + \pi_+\hat{\pi}_0\,\partial_\mu\pi_- - 2\pi_+\pi_-\,\partial_\mu\hat{\pi}_0) + \frac{r^2}{4}m_\pi^2\hat{a}(2\hat{\pi}_0\pi_-\pi_+ + \hat{\pi}_0^3)\right] \quad (2.10)$$

where $A = \frac{1}{3}(1-z)/(1+z) \simeq 0.12$. For the remainder of this paper, we drop the hats and refer to the mass eigenstates as a and π_0. Note that we do not consider the case where m_a and m_π are so highly degenerate that the axion-pion mixing angle becomes of order unity since this does not occur as long as

$$\left|\frac{m_\pi - m_a}{m_\pi}\right| \gtrsim \frac{f_\pi}{f_a} \simeq 10^{-4}\left(\frac{10^3\,\text{GeV}}{f_a}\right) \qquad \begin{pmatrix}\text{Axion-Pion}\\ \text{Non-Degeneracy Condition}\end{pmatrix}, \quad (2.11)$$

which is only violated for axions that are *extremely* degenerate with pions.

The coupling of the axion with photons is

$$\mathcal{L}_{a,\gamma} = \frac{g_\gamma}{4}\frac{a}{f_a}F_{\mu\nu}\tilde{F}^{\mu\nu}, \quad (2.12)$$

$$g_\gamma = \frac{e^2}{8\pi^2}\left(\frac{E}{N} - \frac{5}{3} - \mathcal{F}_\theta(m_a)\right) \quad (2.13)$$

where E/N arises from the UV contribution associated with the anomalies of the PQ symmetry, 5/3 from the axial rotation that removes the axion couplings to gluons, and $\mathcal{F}_\theta$ from axion-meson mixing. For $m_a \ll m_\eta$, $\mathcal{F}_\theta$ reduces to $2\sin\theta f_a/f_\pi$, where θ is the

JHEP04(2024)130

axion-pion mixing angle, (2.9). Further, the value of g_γ in the massless axion case is recovered in the limit $m_a \ll m_\pi$ in which the term in parenthesis reduces to the standard result, $\frac{E}{N} - \frac{2}{3}\frac{4+z}{1+z} \simeq \frac{E}{N} - 2.03$ [51]. For $m_a > m_\pi$, we extract $\mathcal{F}_\theta$ from the calculations of [50] which include $a-\eta$ and $a-\eta'$ mixing. Note that previous considerations of heavy-axion cosmological constraints, except for [45], neglect the effect of axion-meson mixing on $\mathcal{F}_\theta$ which leads to significantly different values of g_γ for $m_a > m_\pi$. Finally, we shall consider two reference values: $E/N = 8/3$, which is the case for the KSVZ model with SU(5) unification, and $E/N = 0$.

3 Computation of the dark radiation density

In this section, we present the numerical results of the Boltzmann equations describing the cosmological evolution of the heavy QCD axion in the early universe. Unlike the standard QCD axion which is light and very long-lived, the heavy QCD axion, with $m_a \gtrsim 1\,\text{MeV}$ and f_a limited by the quality problem, is cosmologically unstable. When the heavy axion decays during or after neutrino decoupling, photons are subsequently heated relative to neutrinos, producing a potentially observable *negative* contribution to ΔN_{eff}. Since the heavy axion can be out of thermal equilibrium around neutrino decoupling and contain a population of axions which have large momenta that decay (dangerously) late, it is crucial to track the momentum space distribution function of the axion, $f_a(\mathbf{p})$, throughout neutrino decoupling.

While neutrino decoupling occurs around the MeV era, the axion often decouples at earlier times and hence its abundance must be traced back to temperatures far above the MeV scale. The dominant interactions between the axion and thermal bath change as the universe cools. For temperatures above the QCD scale, axion-gluon scattering dominates and ensures the axions reach a thermal distribution for sufficiently high temperatures [52] as discussed in section 3.1. For temperatures below the QCD scale, axion-meson scattering and axion-photon scattering can be effective as discussed in section 3.2.

3.1 Axion initial conditions

At temperatures above the QCD phase transition temperature, $T_{\text{QCD}} \approx 150\,\text{MeV}$, axion-gluon interactions may be strong enough to keep the axion in thermal equilibrium. Generally, this process is UV dominated so that for sufficiently high temperatures, the axion reaches thermal equilibrium. As the universe cools, depending on f_a, the axion-gluon interactions may decouple. Likewise, below T_{QCD}, axion-pion interactions may be strong enough to keep the axion in thermal equilibrium. In this subsection, we compute the temperature at which the axion scattering rate with strongly coupled particles decouples, T_{FO}, and in the following subsection we use this freeze-out temperature to set the initial conditions of the axion distribution function of our Boltzmann code, which evolves the axion phase space distribution from temperatures where first-order chiral perturbation theory is valid, $T_{\chi\text{PT}} \equiv 100\,\text{MeV}$ [53] to temperatures past neutrino and electron decoupling. We further discuss the region of parameter space in the (m_a, f_a) plane where perturbation theory in gluon and pion descriptions breaks down at axion decoupling, and quantify the resulting uncertainty in the initial axion abundance.

JHEP04(2024)130

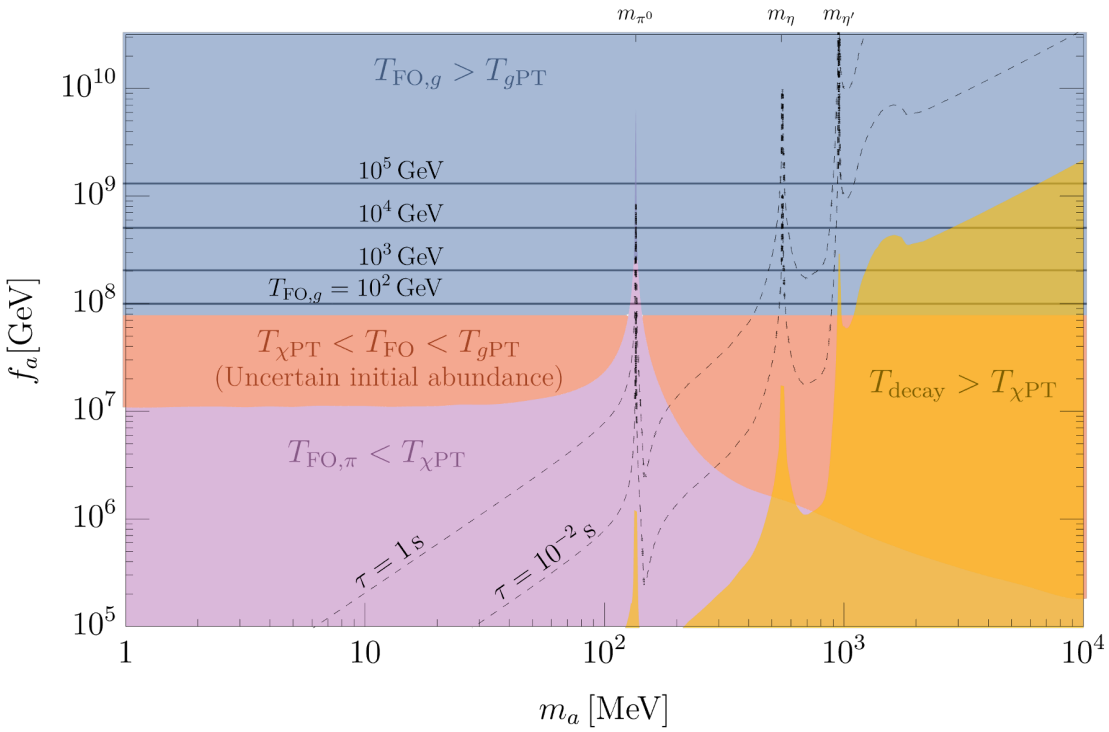

Figure 1. Overview of the parameter space in the $m_a - f_a$ plane where axion interactions with mesons or gluons thermalize. In the purple region, scatterings with pions keep the axion in equilbrium below $T_{\chi\mathrm{PT}}$. In the yellow region, meson or gluon decays and inverse decays keep the axion in equilibrium below $T_{\chi\mathrm{PT}}$. In the blue region, scatterings with gluons once kept the axion in equilbrium. In this region, the horizontal contours denote the gluon freeze-out temperature, $T_{\mathrm{FO,g}}$. The red region indicates where the axions freeze out at temperatures above the validity of chiral perturbation theory ($T_{\chi\mathrm{PT}} \equiv 100\,\mathrm{MeV}$) but below the validity of gluon peturbation theory ($T_{\mathrm{gPT}} \equiv 2\,\mathrm{GeV}$). In this region, the freeze-out temperature is uncertain. In each region, we choose the appropriate initial condition of the axion distribution at $T_{\chi\mathrm{PT}}$; see eq. 3.7 for details.

3.1.1 Equilibrium from scatterings

When the temperature T is much greater than m_a and T_{QCD}, the axion-gluon interaction $a + g \leftrightarrow g + g$ dominates axion production. The thermally averaged rate of axion-gluon scattering is given by [27, 52]

$$\Gamma_{ag\leftrightarrow gg} \simeq \frac{16}{\pi}\left(\frac{g_3^2}{32\pi^2}\right)^2 \frac{T^3}{f_a^2}\mathcal{F}_g(T)\,, \tag{3.1}$$

where $\mathcal{F}_g(T)$ is a temperature-dependent function that captures the axion production enhancement in the plasma from thermal gluon decays. $\mathcal{F}_g(T)$ is numerically computed in [27, 52], and for $g_3 \lesssim 1$, takes the approximate analytic form $\mathcal{F}_g \approx 2g_3^2 \ln 1.5/g_3$ [52, 54].

On the other hand, when $T \lesssim T_{\mathrm{QCD}}$, the interaction $a + \pi \leftrightarrow \pi + \pi$ dominates axion production. The thermally averaged rate of axion-pion scattering is given by

$$\Gamma_{a\pi\leftrightarrow\pi\pi} = \frac{T^5}{f_a^2 f_\pi^2}\frac{A^2}{(1-r^2)^2}\mathcal{F}_\pi(m_a, T) \tag{3.2}$$

JHEP04(2024)130

where $\mathcal{F}_\pi(m_a, T)$ is a temperature and axion mass dependent function that we compute numerically in appendix A. For reference, figure 17 shows $\mathcal{F}_\pi$ as a function of m_π/T for a variety of m_a.

We define the axion decoupling temperature, $T_{\rm FO}$, when $\Gamma_{ag\leftrightarrow gg} = 3H(T_{\rm FO,g})$ for $T \gg T_{\rm QCD}$, or $\Gamma_{a\pi\leftrightarrow\pi\pi} = 3H(T_{\rm FO,\pi})$ for $T \ll T_{\rm QCD}$, where $H(T_{\rm FO})$ is the Hubble rate at $T_{\rm FO}$. Contours of $T_{{\rm FO},g}$ in the $m_a - f_a$ plane are shown by the horizontal lines in the blue-shaded region of figure 1. Likewise, the purple region indicates where the axion-pion freeze-out temperature, $T_{\rm FO,\pi}$ is less than $T_{\chi\rm PT}$. The estimation of $T_{\rm FO,g}$ based on eq. (3.1) breaks down if $m_a > T_{\rm FO,g}$, but we find that it anyway occurs in the red parameter region which possesses greater uncertainty: in the red-shaded region, $T_{\rm FO}$ occurs above the temperature at which chiral perturbation theory breaks down ($T_{\chi\rm PT}$) but below the temperature where the strong coupling constant, g_3, becomes non-perturbative ($T_{g\rm PT}$). We take $T_{\chi\rm PT} \simeq 100\,\text{MeV}$, the temperature above which one-loop corrections in chiral perturbation theory become comparable to tree-level results [53]. Similarly, $T_{g\rm PT} \simeq 2\,\text{GeV}$ is conservatively associated with the energy scale below which g_3 becomes non-perturbative and one-loop corrections become comparable to tree-level results [50]. In the red-shaded region, we cannot precisely determine $T_{\rm FO}$. In section 3.1.3, we evaluate the uncertainty in $N_{\rm eff}$ arising from this uncertainty in $T_{\rm FO}$.

3.1.2 Equilibrium from decays and inverse decays

Even when $T_{\chi\rm PT} < T_{\rm FO} < T_{g\rm PT}$, and hence the freeze-out temperature is uncertain, it is still possible to infer the axion abundance at $T_{\chi\rm PT}$ for sufficiently large m_a. Specifically, if the axion *decay* rate is greater than Hubble at $T_{\chi\rm PT}$, then the axion possesses a thermal distribution at $T_{\chi\rm PT}$. For example, when $m_a \gg T$, the decay $a \to g + g$ can dominate over axion-gluon scattering when $T > T_{g\rm PT}$, or, for example, $a \to 3\pi$ can dominate at $T = T_{\chi\rm PT}$. The axion decay rate to strongly coupled particles is given by

$$\Gamma_{a\to\rm QCD} = \frac{m_a^3}{f_a^2}\mathcal{F}_c(m_a)\,, \tag{3.3}$$

where $\mathcal{F}_c(m_a)$ is an axion mass dependent function that captures the variety of strongly coupled degrees of freedom the axion can decay to. We use $\mathcal{F}_c(m_a)$ as numerically computed in [50], which includes the following meson decay channels: $a \to 3\pi$, $\pi\pi\gamma$, $\eta\pi\pi$, $KK\pi$, $\eta'\pi\pi$, $\rho\rho$, $\omega\omega$, $K^*\overline{K}^*$, and $\phi\phi$. For $m_a \geq T_{g\rm PT}$, the axion to gluon decay rate dominates and $\mathcal{F}_c$ smoothly interpolates to the perturbative result [50]

$$\mathcal{F}_c \simeq \frac{2}{\pi}\left(\frac{g_3^2}{32\pi^2}\right)^2\left(1 + \frac{83g_3^2}{16\pi^2}\right)\,. \tag{3.4}$$

Last, the axion to photon decay rate is given by

$$\Gamma_{a\to\gamma\gamma} = \frac{g_\gamma(m_a)^2}{64\pi}\frac{m_a^3}{f_a^2}\,, \tag{3.5}$$

where $g_\gamma(m_a)$ is given in (2.13). Note that $g_\gamma(m_a)$ is a function of the axion mass due to the effects of axion-meson mixing as encoded in the mixing function $\mathcal{F}_\theta(m_a)$.

We define the axion decay temperature, $T_{\rm decay}$, when $\Gamma_{a\to\rm QCD} + \Gamma_{a\to\gamma\gamma} = 3H(T_{\rm decay})$. The yellow region of figure 1 shows the region where $T_{\rm decay} > T_{\chi\rm PT}$. In this region, the

JHEP04(2024)130

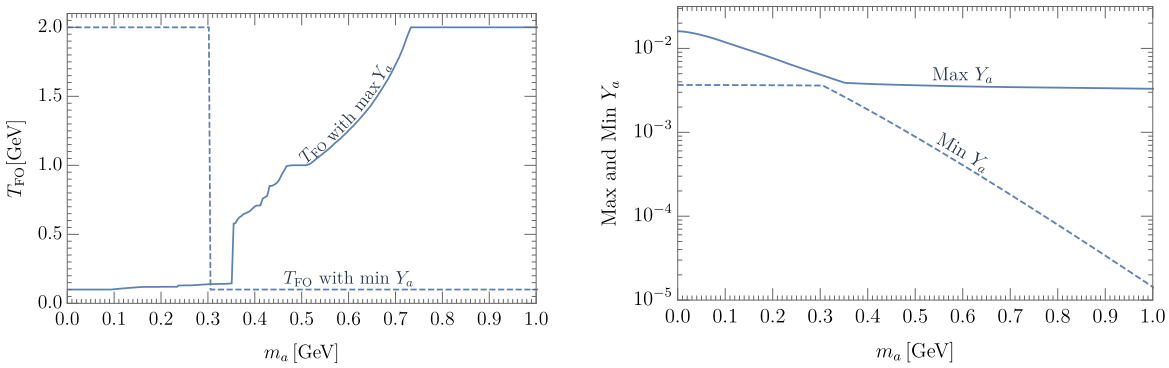

Figure 2. When $T_{\chi\rm PT} < T_{\rm FO} < T_{\rm gPT}$, the initial axion density at the start of the Boltzmann code is uncertain. The left panel bounds this uncertainty by showing the two extreme $T_{\rm FO} \in (T_{\chi\rm PT}, T_{\rm gPT})$ that give the largest (solid) and smallest (dashed) axion densities at the starting temperature of the Boltzmann code. The right panel shows the corresponding axion yields. The cross-over between the maximum and minimum $T_{\rm FO}$ around 0.3 GeV arises from the balance between Boltzmann suppression and dilution by g_* across the QCD phase transition.

axion possesses a thermal distribution when we begin our Boltzmann code at $T_{\chi\rm PT}$, even if $T_{\rm FO}$ is uncertain.

Note that if the axion decays far before or after neutrino decoupling, the initial condition of the axion at $T_{\chi\rm PT}$ becomes insensitive to the calculation of $\Delta N_{\rm eff}$. In particular, below the lower dashed line, $\Gamma_a = \Gamma_{a\to\rm QCD} + \Gamma_{a\to\gamma\gamma}$, is so large that the axion always decays before the universe is 10^{-2} seconds old. In this region, the neutrinos are still strongly coupled to the thermal bath when the axion decays so that any effect to $\Delta N_{\rm eff}$ from the axion is erased, regardless of the initial axion abundance at $T_{\chi\rm PT}$. Likewise, above the upper dashed line. Γ_a is so small that the axion always decays after the universe is 1 second old. In this region, neutrinos have long since decoupled from the thermal bath when the axion decays, leading to $\Delta N_{\rm eff} \ll -0.3$, which is already excluded by the observations of CMB [19].

3.1.3 Initial condition and its uncertainty

For (m_a, f_a) in the purple or yellow regions of figure 1, the axion is in thermal equilbrium at $T_{\chi\rm PT}$. Consequently, in these regions, we take the initial distribution function of the axion at $T_{\chi\rm PT}$ to be a Bose-Einstein distribution of temperature $T_{\chi\rm PT}$. For sufficiently large f_a, however, the axion decouples from the bath at $T_{\rm FO} > T_{\chi\rm PT}$ (blue region), and we take the initial axion distribution to be a thermal one at $T_{\rm FO}$, red-shifted down to $T_{\chi\rm PT}$. Inside the red-shaded region, however, $T_{\rm FO}$ is uncertain. Despite this uncertainty, we can still bound $\Delta N_{\rm eff}$ by running our axion Boltzmann code with both the maximum and minimum possible axion abundance at $T_{\chi\rm PT}$. We scan over possible freeze-out temperatures between $T_{\chi\rm PT}$ and $T_{g\rm PT}$ for all axion masses in the red-shaded region to determine the smallest and largest abundance at $T_{\chi\rm PT}$ as a function of m_a. In figure 2, the left panel shows the $T_{\rm FO}$ that gives the maximum (blue) and minimum (orange) axion yield, $Y_a = n_a/s$, as a function of m_a, and the right panel shows these maximum and minimum yields. Note that the smallest possible axion number density is *not* necessarily that of an axion in thermal equilibrium at $T_{\chi\rm PT}$ and the largest that of a frozen-out abundance at $T_{\rm FO} = T_{g\rm PT}$. This is because

JHEP04(2024)130

large changes in the degrees of freedom of the thermal bath between $T_{\chi\mathrm{PT}}$ and $T_{g\mathrm{PT}}$ can dilute the previously frozen-out axion. For all future plots, we show the results of ΔN_{eff} arising from these two possible initial conditions.

In summary, we take the initial axion distribution function at $T_{\chi\mathrm{PT}}$ (time $t_{\chi\mathrm{PT}}$) to be

$$f_a(\mathbf{p}_a, t = t_{\chi\mathrm{PT}}) = \left(\exp\frac{\sqrt{|\mathbf{p}_*|^2 + m_a^2}}{T_*} - 1\right)^{-1}, \quad |\mathbf{p}_*| = |\mathbf{p}_a|\frac{a(T_*)}{a(T_{\chi\mathrm{PT}})} \tag{3.6}$$

where $f_a(\mathbf{p}_a)$ is a Bose-Einstein distribution with momentum $\mathbf{p}_a$ and effective temperature T_* given by

$$T_* = \begin{cases} T_{\mathrm{FO},g} & \text{if } T_{\mathrm{FO}} \geq T_{g\mathrm{PT}} \\ T_{\chi\mathrm{PT}} & \text{if } T_{\mathrm{FO}} \leq T_{\chi\mathrm{PT}} \text{ or } T_{\mathrm{decay}} \geq T_{\chi\mathrm{PT}} \\ \text{Max \& Min } T_{\mathrm{FO}} \text{ (see figure 2)} & \text{if } T_{\chi\mathrm{PT}} < T_{\mathrm{FO}} < T_{g\mathrm{PT}} \text{ and } T_{\mathrm{decay}} < T_{\chi\mathrm{PT}} \end{cases} \tag{3.7}$$

Note that if $T_{\mathrm{RH}} < T_*$ or if there is a source of dilution in the universe after the axion freezes-out, then the initial abundance of axions can be small and the bounds on N_{eff} discussed in this work are weakened.

3.2 Axion abundance below Λ_{QCD}: Boltzmann equations

Accurately capturing the effect of heavy axion decoupling and decay on our cosmology requires understanding the phase space evolution of the axion in the primordial thermal bath. The Boltzmann equation describing the evolution of the axion phase space density, $f_a(\mathbf{p}_a)$, is

$$\frac{\partial f_a}{\partial t} - p_a H \frac{\partial f_a}{\partial p_a} = (C_\gamma + C_P + C_\pi + C_\Gamma)(f_{a,\mathrm{eq}} - f_a), \tag{3.8}$$

where $p_a = |\mathbf{p}_a|$ is the magnitude of the axion momentum, H is the Hubble expansion rate, and C_γ, C_P, C_π, and C_Γ are the collision terms for axion-two photon scattering, axion-Primakoff scattering, axion-pion scattering, and axion-meson decay, respectively.

Generally, the collision term, C, corresponding to the axion interaction $a + A + B + \ldots \leftrightarrow I + J + \ldots$, is

$$\begin{aligned} &C(f_{a,\mathrm{eq}} - f_a) \\ &= \frac{1}{2E_a}\int d\Pi_A d\Pi_B \ldots d\Pi_I \ldots d\Pi_J \ldots S\,|\mathcal{M}|^2 \Lambda\,(2\pi)^4 \delta^4(p_a + p_A + p_B \ldots - p_I - p_J \ldots) \end{aligned} \tag{3.9}$$

where $E_a = \sqrt{p_a^2 + m_a^2}$ is the axion energy, $d\Pi = d^3p/(2\pi)^3 2E$ is the phase space measure per particle, $|M|^2$ is the matrix element of the interaction, $S = 1/m!$ is the symmetry factor for every m identical particles in the initial or final states, and

$$\begin{aligned} \Lambda &= [(1 \pm f_A)(1 \pm f_B)\ldots(1 \pm f_a) f_I f_J \ldots - f_A f_B \ldots f_a(1 \pm f_I)(1 \pm f_J)\ldots] \\ &\simeq (f_{a,\mathrm{eq}} - f_a)\exp(-E_A/T)\exp(-E_B/T)\ldots \quad \text{(Kinetic equilibrium limit)} \end{aligned} \tag{3.10}$$

is the phase space density factor for all the incoming and outgoing particles interacting with the axion, where the plus sign refers to stimulated emission (boson) and the minus to Fermi blocking (fermion). The second line of eq. (3.10) shows Λ in the limit where $1 \pm f \simeq 1$

JHEP04(2024)130

with $f = \exp(-E/T)$ the Boltzmann distribution, which is an excellent approximation for particles in kinetic equilibrium.

In past literature, only the axion-two photon, C_γ, and the axion-Primakoff, C_P, collision terms have been considered in calculations involving the axion Boltzmann equation. Consequently, these terms have already been computed, and their values are [55]

$$C_\gamma \approx \frac{m_a^2 - 4m_\gamma^2}{m_a^2}\frac{m_a}{E_a}\left[1 + \frac{2T}{p_a}\log\frac{1-e^{-(E_a+p_a)/2T}}{1-e^{-(E_a-p_a)/2T}}\right]\Gamma_{a\to\gamma\gamma} \tag{3.11}$$

$$C_P \approx \frac{\Gamma_{a\to\gamma\gamma}}{m_a^3}\sum_{i=e,\mu,\pi_\pm} n_i e_i^2 \log\left[1 + \frac{16E_a^2(m_i+3T)^2}{m_\gamma^2(m_i^2+(m_i+3T)^2)}\right]. \tag{3.12}$$

Here, $\Gamma_{a\to\gamma\gamma}$ is the axion-to-two photon decay rate, (3.5), m_γ is the photon plasma mass, and n_i is the number density of the ith electromagnetically charged particle of charge e_i in the thermal bath. When the electron is relativistic, $m_\gamma \simeq eT/3$ [56], but when the electron becomes non-relativistic at $T \lesssim m_e$, m_γ reduces to the classical plasma frequency of $m_\gamma \simeq e\sqrt{n_e/m_e}$, which is exponentially suppressed. For simplicity, we piecewise-connect the two regimes for m_γ when they intersect, which occurs roughly at $T \simeq m_e/2$.

The axion-pion scattering collision term for a massive axion has not been computed in the literature and we do so for the first time in appendix A. C_π takes the form

$$C_\pi = \left(\frac{A}{f_a f_\pi}\frac{1}{1-r^2}\right)^2 \frac{T^6}{2E_a} \times \mathcal{F}_{\rm PS}\left(\frac{m_a}{T}, \frac{p_a}{T}\right), \tag{3.13}$$

where $A = \frac{1}{3}(1-z)/(1+z) \simeq 0.12$ and $r \equiv m_a/m_\pi$ as before. The function $\mathcal{F}_{\rm PS}$ contains the phase space integration over the axion-pion scattering matrix. In appendix A, we determine this axion-pion scattering matrix, numerically perform the phase integration, and show how C_π agrees with the massless axion result found in literature [53, 57]. Note that integration of C_π over the axion phase space defines $\Gamma_{a\pi\leftrightarrow a\pi}$ given in eq. (3.2).

The axion-meson decay collision term has also never been considered in the literature. Under the Boltzmann approximation in the kinetic equilbrium limit, C_Γ is simply

$$C_\Gamma \approx \frac{m_a}{E_a}\Gamma_{\rm QCD}\,, \tag{3.14}$$

where $\Gamma_{\rm QCD}$ is the total axion decay rate to all final states containing mesons (3.3). In (3.14), we use the Boltzmann kinetic equilibrium approximation.

It is fruitful to estimate the impact of the axion-pion scattering and axion-meson decays compared with the standard Boltzmann calculations in literature which only include Primakoff scattering and axion-photon decays. For example, the solid contours in figure 3 show the axion-pion decoupling temperature, $T_{{\rm FO},\pi}$ vs f_a over a range of axion masses. For $f_a \lesssim 10^6\,{\rm GeV}$, the axion remains in thermal equilibrium from pionic interactions until a few 10s of MeV which is typically far lower than the Primakoff decoupling temperature [18],

$$T_{\rm FO,P} \approx 91\,\frac{\sqrt{g_*(T_{\rm FO,P})}}{g_c(T_{\rm FO,P})}\left(\frac{f_a}{10^6\,{\rm GeV}}\right)^2\left(\frac{g_\gamma}{\alpha/2\pi}\right)^{-2}\,{\rm GeV}\,, \tag{3.15}$$

JHEP04(2024)130

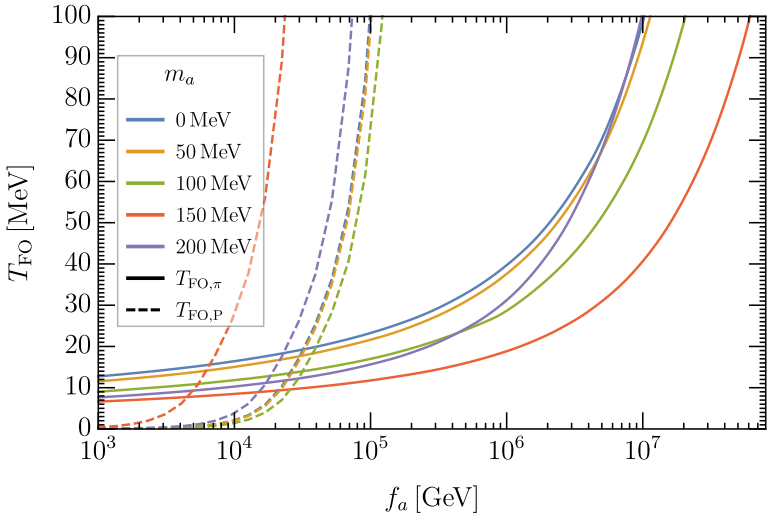

Figure 3. (Left) Axion freeze-out temperature from pion (solid) and Primakoff (dashed) scatterings as a function of f_a for a variety of m_a between 0 and 200 MeV. For $f_a \gtrsim 3 \times 10^4$ GeV, the axion-pion scattering dominates over Primakoff scattering, keeping the axions in thermal equilbrium until $T \sim 10$ MeV for $f_a \lesssim 10^6$ GeV.

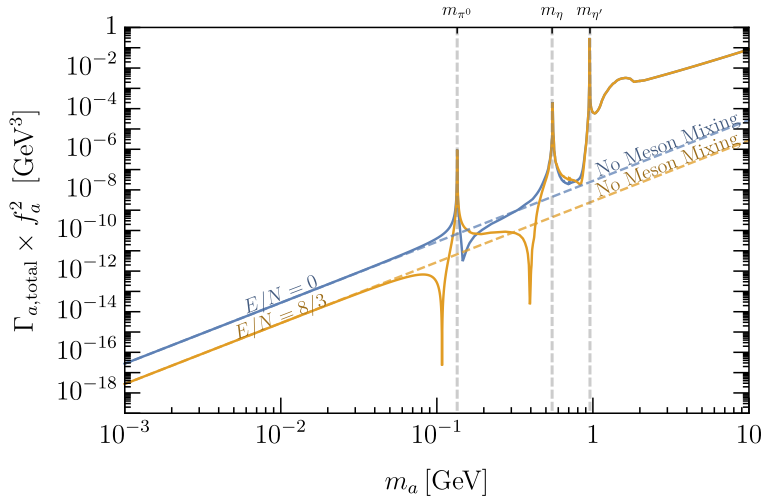

Figure 4. (Right) Total axion decay rate (τ^{-1}) as a function of m_a for $E/N = 0$ (blue) and $E/N = 8/3$ (orange). Resonant peaks in the decay rate arise from axion-meson mixing when m_a is near m_{π^0}, m_η, and m'_η. Troughs arise from cancellations in g_γ between the anomaly, axial rotation, and meson-mixing contributions. For $m_a \gtrsim 2$ GeV, the decay rate is set by gluons. The dashed contours show the axion-photon decay rate without meson mixing.

JHEP04(2024)130

where g_c is the sum of the charged relativistic degrees of freedom in the bath. The Primakoff decoupling temperature is shown by the dashed contours in the left panel of figure 3. For $f_a \gtrsim 5 \times 10^4\,\text{GeV}$, $T_{\text{FO,P}} \gg T_{\text{FO},\pi}$, demonstrating the importance of the pions at maintaining thermal equilibrium with the axion all the way to $O(10)\,\text{MeV}$ temperatures. The lower pionic decoupling temperature compared to standard Primakoff decoupling leads to two important effects: (1) it can reduce the abundance of axions with masses above $T_{\text{FO},\pi}$, as they now follow an exponentially suppressed distribution relative to the standard, non-Boltzmann suppressed distribution; and (2) it can enhance the initial abundance of axions with masses below $T_{\chi\text{PT}}$ as they are not diluted by g_{*S} like axions that decouple from Primakoff interactions in the early universe.

Similarly, axion-meson decays and inverse decays can keep the axion in thermal equilbrium at low temperatures. Most importantly, for a fixed f_a, the additional QCD decay channels can significantly decrease the axion lifetime relative to $\Gamma^{-1}_{a\to\gamma\gamma}$, which is the standard axion lifetime taken in previous Boltzmann calculations. For example, the solid blue and orange contours of figure 4 show the total axion decay rate including QCD decay channels for $E/N = 0$ and $8/3$, respectively. Compared to the dashed contours used in past literature, which show $\Gamma_{a\to\gamma\gamma}$ when meson mixing and QCD channels are absent, the realistic total axion decay rate can be significantly different. Moreover, because the axion lifetime relative to neutrino decoupling dominantly sets the N_{eff} signal, we expect that incorporating axion-to-QCD channels will significantly alter the allowed parameter space in the (m_a, f_a) plane.

To precisely quantify these new effects, the phase space evolution of the axion, (3.8), together with the evolution of the Standard Model particles in the thermal bath must be computed to determine the effect of axion decoupling and decay on the relative temperature differences between photons and neutrinos in our present Universe, as typically characterized by the effective number of neutrino species

$$N_{\text{eff}} = \frac{8}{7}\left(\frac{11}{4}\right)^{4/3}\frac{\rho_\nu}{\rho_\gamma}\,. \tag{3.16}$$

Here, ρ_ν and ρ_γ are the neutrino and photon energy densities. Note that N_{eff} is most sensitive to heavy axions that decay at temperatures near neutrino decoupling, which occurs around the MeV scale. The particles in the thermal bath from $T_{\chi\text{PT}}$ through neutrino decoupling are photons, neutrinos, electrons, muons, pions and a small density of heavier mesons. The contribution to the energy density from these heavier mesons and from deviations of pions from the ideal gas law from self-interactions, $\rho_{\delta_{\text{QCD}}}$, is approximately 5% of the total energy density at $T_{\chi\text{PT}}$ and quickly drops far below 1% by $T = 60\,\text{MeV}$ (see figure 18).

The evolution of the energy density of species in the thermal bath that are tightly thermally coupled follows the energy density Boltzmann equation

$$\begin{aligned}\sum_{i=\gamma,e,\mu,\pi,\delta_{\text{QCD}}}\frac{\partial\rho_i}{\partial t} + 3H(\rho_i + P_i) = \frac{\Gamma_{\nu e}}{T^4}(\rho^2_{\nu_e} - \rho^2_{\nu_e,\text{eq}}) + \frac{\Gamma_{\nu_{\mu\tau}}}{T^4}(\rho^2_{\nu_{\mu\tau}} - \rho^2_{\nu_{\mu\tau},\text{eq}}) \\ + \int\frac{d^3p_a}{(2\pi)^3}\sqrt{p_a^2 + m_a^2}(C_\gamma + C_P + C_\pi + C_\Gamma)(f_a - f_{a,\text{eq}}),\end{aligned} \tag{3.17}$$

JHEP04(2024)130

where

$$\rho_i = \int \frac{d^3p_i}{(2\pi)^3}\sqrt{p_i^2+m_i^2}\, f_i(p_i), \qquad P_i = \int \frac{d^3p_i}{(2\pi)^3}\frac{1}{3}\frac{p_i^2}{\sqrt{p_i^2+m_i^2}}\, f_i(p_i) \tag{3.18}$$

are the energy densities and pressures of the ith tightly coupled species in the bath. We assume that the photons and pions follow Bose-Einstein distributions and the electrons and muons follow Fermi-Dirac distributions. As discussed more in appendix C, we infer $\rho_{\delta_{\rm QCD}}$ and $P_{\delta_{\rm QCD}}$ from the work of [58], which computes the Standard Model equation of state across the QCD phase transition and takes into account the deviations from the ideal gas law arising from the strongly coupled QCD bath.

The energy densities of particles not strongly thermally coupled electromagnetically, namely the axion and neutrinos, must be solved for numerically. Specifically, the rate of change of the neutrino energy densities on the right side of (3.17) follow the Boltzmann equations

$$\frac{\partial\rho_{\nu_e}}{\partial t} + 4H\rho_{\nu_e} = -\frac{\Gamma_{\nu e}}{T^4}(\rho_{\nu_e}^2 - \rho_{\nu_e,\rm eq}^2) \tag{3.19}$$

$$\frac{\partial\rho_{\nu_{\mu\tau}}}{\partial t} + 4H\rho_{\nu_{\mu\tau}} = -\frac{\Gamma_{\nu_{\mu\tau}}}{T^4}(\rho_{\nu_{\mu\tau}}^2 - \rho_{\nu_{\mu\tau},\rm eq}^2). \tag{3.20}$$

Here, $\Gamma_{\nu_e} \simeq 0.68\, G_F^2 T^5$ and $\Gamma_{\nu_{\mu\tau}} \simeq 0.15\, G_F^2 T^5$ [18] are thermally averaged neutrino interaction rates with the thermal bath for electron neutrinos and for muon and tau neutrinos, respectively.

Last, the Hubble rate, H, quantifies the expansion rate of the universe and sets the decoupling time of all interactions. The squared Hubble rate is set by the sum of all energy densities,

$$H^2 = \left(\frac{\dot R}{R}\right)^2 = \frac{8\pi G}{3}\left(\rho_\gamma + \rho_e + \rho_\mu + \rho_\pi + \rho_{\delta_{\rm QCD}} + \rho_{\nu_e} + \rho_{\nu_{\mu\tau}} + \rho_a\right). \tag{3.21}$$

We numerically solve the system of equations (3.8)–(3.21) using the method of lines [59]. The method of lines is a numerical technique for solving a system of partial differential equations by discretizing one independent variable direction (comoving momentum in our case) while keeping the other independent variable continuous (logarithmic time in our case). The main advantage of the method of lines technique is the conversion of the Boltzmann system of *partial* differential equations in $\{|\mathbf{p}_a|, t\}$ into a system of many *ordinary* differential equations in $\{t\}$ which is computationally easier to solve. Moreover, by keeping the time-like variable continuous, useful techniques such as dynamical step-sizes can be employed to speed up the computation by automatically taking large temporal time-steps when changes in the interactions are small (such as at thermal equilibrium) while taking small temporal time-steps when changes are sudden (such as decays, decouplings, or re-thermalizations). See appendix C for more details of our numerical setup.

3.3 $\Delta N_{\rm eff}$

In this section, we present the numerical results of $N_{\rm eff}$ as determined from the Boltzmann equations of section 3.2 describing the cosmological evolution of the heavy QCD axion below $T_{\chi\rm PT}$.

JHEP04(2024)130

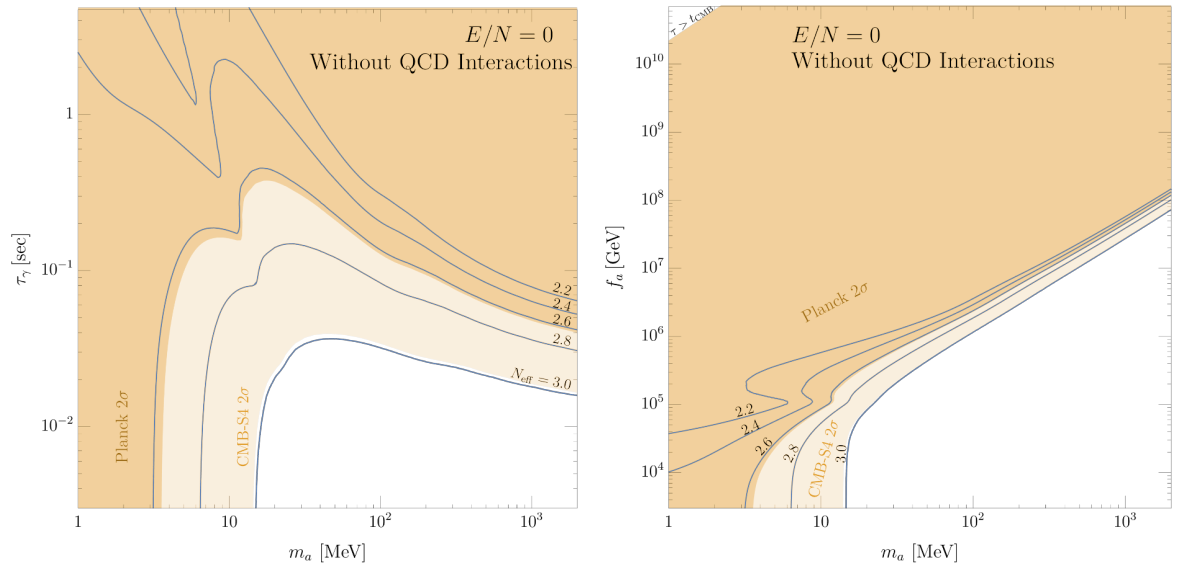

Figure 5. Contours of $N_{\rm eff}$ in the $m_a - \tau_\gamma$ (left) and $m_a - f_a$ (right) planes *neglecting* the following crucial effects that we take into account in future figures: axion-pion scattering, axion-meson decays, axion-meson mixing in g_γ, the proper frozen-out initial axion abundance, and the QCD contributions to the background evolution. Note that by neglecting these effects, as done in past works, the axion-lifetime is incorrectly set by the axion-photon decay rate with no axion-meson mixing, as shown by the y-axis of the left panel. The dark orange region is excluded at 95% confidence by Planck, while the light orange shows the future reach of CMB-S4 experiment at 95% confidence.

First, to compare with past literature and highlight the importance of the new effects discussed in this work, we show $N_{\rm eff}$ for heavy axion cosmologies *without* incorporating the following crucial elements in the Boltzmann code: axion-pion scattering, axion-meson decay, axion-meson mixing in g_γ, the proper frozen-out initial axion abundance, and the QCD contributions to the background energy density as described by ρ_π and $\delta_{\rm QCD}$. Figure 5 shows the numerical results of $N_{\rm eff}$ when these terms are neglected. That is, including only the photon (C_γ) and Primakoff (C_P) collision terms in eq. (3.8) and eq. (3.17); including only γ, e and μ in the sum of the thermally coupled species of eq. (3.17); including only $\rho_\gamma, \rho_e, \rho_\mu, \rho_{\nu_e}, \rho_{\nu_{\mu\tau}}$, and ρ_a in Hubble (3.21); setting the initial abundance of axions at the start of the Boltzmann code to that of a frozen-out abundance set by Primakoff scatterings such that $T_* = {\rm Max}(T_{\rm FO,P}, T_{\chi{\rm PT}})$; and finally, in eq. (2.13), setting $E/N = 0$ and $\mathcal{F}_\theta = (1-z)/(1+z)$, which is the axion-meson mixing contribution in the inapplicable $m_a \ll m_\pi$ limit. The left panel of figure 5 shows contours of $\Delta N_{\rm eff}$ in the $m_a - \tau_\gamma$ plane, where τ_γ is the axion to photon lifetime when axion-meson mixing is neglected. Note that τ_γ is the total lifetime of the axion since QCD decay channels are neglected in this particular case.

For $\tau_\gamma \gtrsim 10^{-1}$ s the axion decays after neutrino decoupling, heating up the photons relative to the neutrinos and giving rise to $\Delta N_{\rm eff} < 0$ as can be seen from the enhanced denominator of eq. (3.16). For $\tau_\gamma \lesssim 10^{-1}$ s and $m_a \gtrsim 10\,{\rm MeV}$, the axion decays sufficiently early that the photons and neutrinos rethermalize before the neutrino decouples. In this scenario, the $N_{\rm eff}$ signal of the heavy axion is absent and $\Delta N_{\rm eff} \simeq 0$. For $\tau_\gamma \lesssim 10^{-1}$ s and $m_a \lesssim 10\,{\rm MeV}$, the axion remains in thermal equilibrium past neutrino decoupling, heating

JHEP04(2024)130

up the photons and again giving rise to negative $\Delta N_{\rm eff}$. The right panel of figure 5 shows the same $\Delta N_{\rm eff}$ contours as the left panel but in the $m_a - f_a$ plane. Both panels assume the usual hadronic axion with $E/N = 0$. Taking the GUT motivated value of $E/N = 8/3$ only slightly shifts the contours in the right panel vertically.

We now consider $N_{\rm eff}$ for heavy axion cosmologies incorporating the new effects included in this work: axion-pion scattering, axion-meson decay, axion-meson mixing in g_γ, the proper (and occasionally uncertain) frozen-out initial axion abundance, the QCD contributions to the background energy density as described by ρ_π and $\delta_{\rm QCD}$, as well results for the KSVZ $E/N = 0$ and the GUT motivated $E/N = 8/3$. Figures 6 and 7 show the contours of $\Delta N_{\rm eff}$ for heavy axions with these additional contributions for $E/N = 0$ (KSVZ) and $E/N = 8/3$ (GUT), respectively. In both figures, the left and right panels show the parameter space in the (m_a, τ) and (m_a, f_a) planes, respectively. Note that here, τ is the *total* lifetime of the axion, which begins differing from τ_γ for $m_a \gtrsim m_\pi$ where axion-meson mixing becomes important and then becomes even more disparate when axion-meson channels open for $m_a \gtrsim 3m_\pi$, as shown in figure 4. The solid and dashed blue contours in each panel correspond to taking the maximum possible Y_a (blue) and minimum possible Y_a (dashed) when $T_{\rm FO}$ lies in the uncertain region between $T_{\chi{\rm PT}}$ and $T_{g{\rm PT}}$, as indicated in figure 2. The separation between the solid and dashed blue contours indicates the uncertainty in $N_{\rm eff}$ arising from the uncertainty in $T_{\rm FO}$ in this region. As can be seen, this region is localized roughly between $250\,{\rm MeV} \lesssim m_a \lesssim 800\,{\rm MeV}$ and, for any value of m_a in this region, the uncertainty in the value of f_a for any $N_{\rm eff}$ contour is typically only a several 10s of percent and always less than a factor 3.

Figures 6 and 7 demonstrate three important differences in the $N_{\rm eff}$ signal from heavy axions as currently considered in literature (figure 5): first, the effect of axion-pion resonance on the mixing angle can be seen by the triangular shaped peaks near $m_a = m_\pi^0$. In this regions, the axion is tightly coupled thermally to pions so that when the axion decays, its abundance is sufficiently exponentially suppressed that it does not heat up the photons even when decaying past neutrino decoupling. Second, for $m_a \gtrsim 3m_\pi$, $|\Delta N_{\rm eff}|$ is reduced for fixed (m_a, f_a) due to the meson-decay channels now open which cause the axion to decay earlier, especially near resonances in the mixing angle at $m_a = m_\pi$, m_η, and $m_{\eta'}$. This can be seen more clearly in the (m_a, f_a) planes. Note that for some m_a, incorporating axion-meson mixing can *increase* the axion lifetime due to cancellations between contributions of g_γ (3.5). The increased $|\Delta N_{\rm eff}|$ for fixed (m_a, f_a) due to the increased axion lifetime is important for $m_a < 3m_\pi$ when only the axion-photon decay channel is open. Third, for $m_a \lesssim m_\pi$, $|\Delta N_{\rm eff}|$ is reduced for fixed (m_a, f_a) because the axion is kept in thermal equilibrium by axion-pion scattering to lower temperatures compared to when the pions are absent. This leads to a reduced axion abundance at neutrino decoupling which reduces the $|\Delta N_{\rm eff}|$ contribution from the axion.

Each of these effects can be seen more clearly in the top panels of figure 8 which show the evolution of the energy densities of the axion and other species in the thermal bath as a function of time and temperature (top horizontal axis) for fixed $(m_a,\ f_a) = (100\,{\rm MeV},\ 2.5\times10^6\,{\rm GeV})$ and $(1000\,{\rm MeV},\ 1.0\times10^9\,{\rm GeV})$, in the top left and top right panels, respectively. The dark colored contours show the evolution of the comoving energy density, $X_i = \rho_i R^4$ of the ith species when including the axion-meson interactions while the light colored contours show the same evolution when the axion-meson interactions are absent. The electromagnetic

JHEP04(2024)130

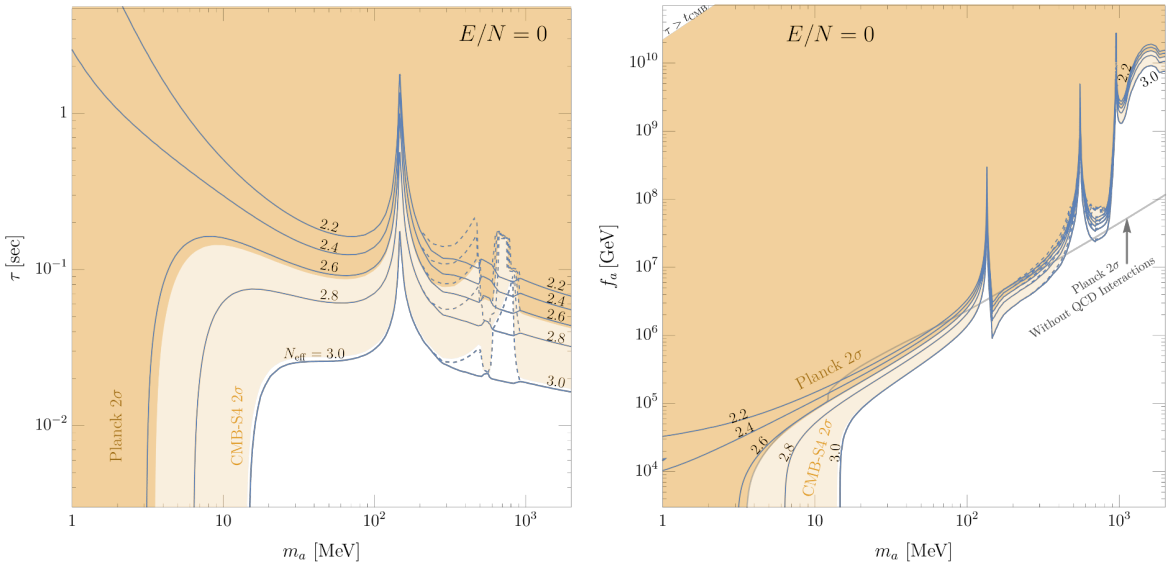

Figure 6. Contours of $N_{\rm eff}$ in the $m_a - \tau$ (left) and $m_a - f_a$ (right) planes for $E/N = 0$. The dark orange region is excluded at 95% confidence by Planck, while the light orange shows the future reach of CMB-S4 experiment at 95% confidence. The dashed contours indicate where the initial axion yield is uncertain because $T_{\rm FO}$ lies between $T_{\chi \rm PT}$ and $T_{\rm gPT}$. The dashed contours bound this uncertainty by showing the value of $N_{\rm eff}$ taking the minimum initial axion yield while the solid contours show the value of $N_{\rm eff}$ taking the maximum initial axion yield as given in figure 2.

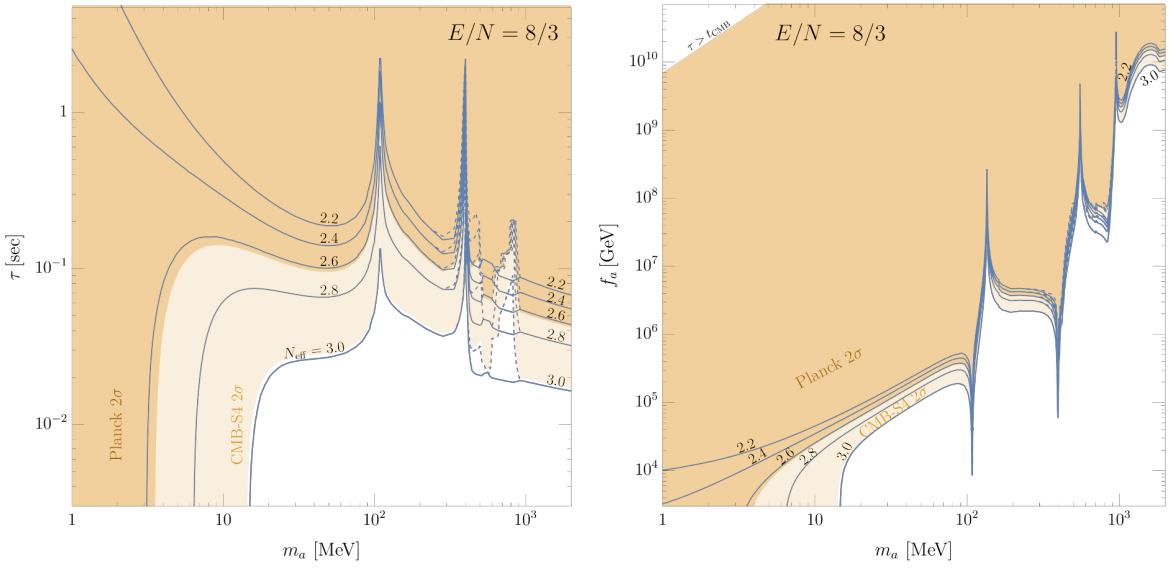

Figure 7. Same as figure 6, but for E/N = 8/3.

JHEP04(2024)130

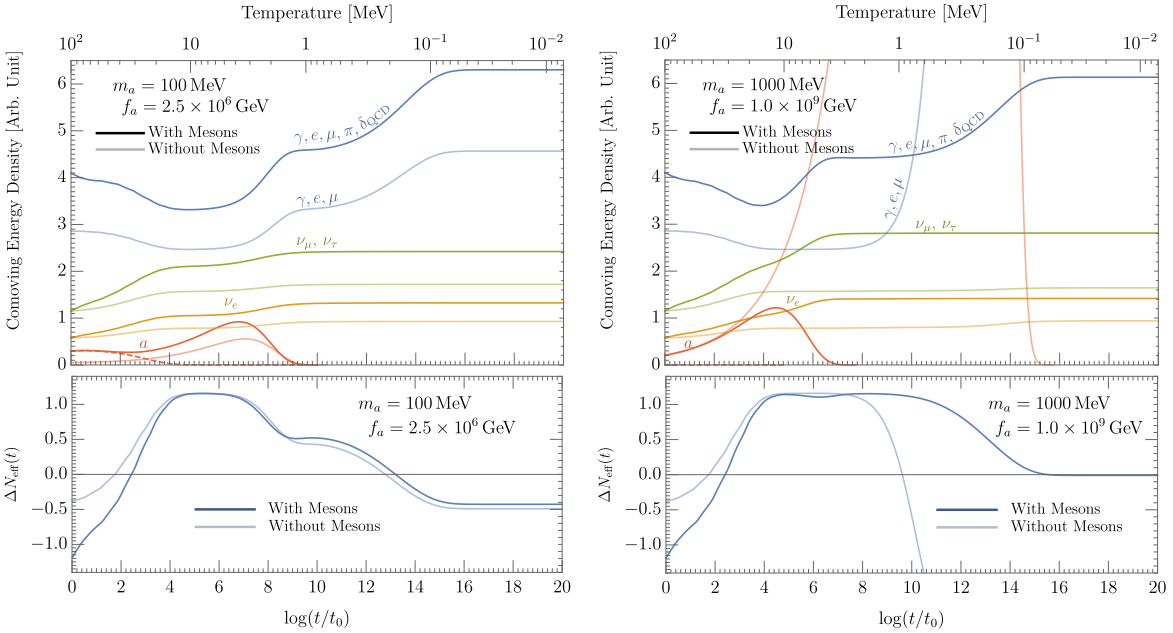

Figure 8. Top panels show the comoving energy density evolution of the axion (dark red), electron neutrinos (dark orange), muon and tau neutrinos (dark green), and strongly coupled species in the Standard Model thermal bath (dark blue) for $(m_a, \tau) = (100\,\text{MeV}, 0.1\text{s})$, left, $(m_a, \tau) = (1000\,\text{MeV}, 0.1\text{s})$, right. The correspondingly lighter shaded contours show the same evolution but without pion or meson interactions. The dashed red contour shows the axion comoving energy density if it were to maintain a thermal density at all times. The bottom panels show the instaneous value of eq. (3.16) minus the Standard Model result, $N_{\text{eff}}^{\text{SM}} = 3.044$. The left and right panels respectively highlight how including QCD interactions can keep the axion thermally coupled to the Standard Model bath for a longer time or enhance the axion decay rate at a fixed f_a. The left panel demonstrates that for low m_a, the axion can be in thermal equilbrium at $T_{\chi\text{PT}}$ when including pions-interactions but be out of equilbrium when including only Primakoff processes which freeze-out at much higher temperatures that lead the axion to possess a g_{*S} diluted abundance at $T_{\chi\text{PT}}$. In the left panel, the axion lifetime with or without mesons is approximately the same ($\tau \approx 0.1$ s) because the meson decay channels are forbidden and axion-pion mixing is not too appreciable yet. In contrast, the right panel demonstrates that for high m_a, the axion can decay much earlier due to the kinematic availability of meson decay channels ($\tau \approx 0.01$ s with meson interactions and 24 s without). This leads to a reduced ΔN_{eff}, as shown on the bottom right panel. In both panels, we take $E/N = 0$.

component of the thermal bath, $\gamma, e, \mu, \pi, \delta_{\text{QCD}}$ is shown in blue, $\nu_{\mu,\tau}$ in green, ν_e in orange, and the axion in red. The dashed red contour shows the comoving energy density of the axion if it were to maintain a thermal distribution for all times. As can be seen from the $m_a = 100\,\text{MeV}$ panel, the axion starts off in thermal equilbrium compared to the case without meson interactions in which the axion possesses a g_{*S} suppressed abundance from earlier Primakoff freeze-out. Moreover, the axion abundance with meson interactions follows the dashed thermal distribution to lower temperatures than without meson interactions. This leads to a relative suppression in the non-relativistic abundance of the axion prior to decaying around 2 MeV. Consequently, including axion-pion scattering ΔN_{eff} is not as negative as previous results in the literature. The temporal evolution of $\Delta N_{\text{eff}}(t) = N_{\text{eff}}(t) - 3.044$, as

JHEP04(2024)130

shown by the dark blue (with mesons) and light blue (without mesons) contours in the lower left panel of figure 8, demonstrates this difference explicitly. Note that for $m_a = 100\,\text{MeV}$, the axion mass is on the cusp of the axion-pion resonance for $E/N = 0$. For m_a closer to m_π, the axion follows the dashed thermal abundance for a longer duration which generates the large triangular peak in the allowed N_{eff} plot of figure 6.

For $m_a = 1000\,\text{MeV}$, the axion with meson interactions again follows the dashed thermal distribution to slightly lower temperatures than the axion without meson interactions. More important though is the difference in decay time between the two cases. In particular, the axion with meson interactions (dark red) decays earlier than the axion without (light red) due to the $a \to \eta\pi\pi, \pi\pi\gamma$ decay channels that are now kinematically open to the 1000 MeV axion that are absent from the 100 MeV axion. These extra decay channels lead to a much smaller ΔN_{eff} as shown explicitly by the evolution of ΔN_{eff} in the bottom right panel of figure 8.

We note that for $m_a > 2\,\text{GeV}$, the axion decays dominantly into gluons. Here, the 2σ limit on N_{eff} as constrained by Planck approximately follows the contour $\tau \approx 0.05$ s around $m_a \sim \text{GeV}$ and slowly drops with increasing axion mass. The slight decrease in the maximum allowed τ in this region originates from the increase in the axion energy density at decay with axion mass: for such heavy axions with long lifetimes, f_a is large and the axion freezes-out early, leading to freeze-out yield roughly independent of m_a. Consequently, the heavier the axion, the earlier it must decay so that its energy density at neutrino decoupling is further exponentially suppressed to counter its larger frozen-out energy density. As shown in appendix B, the exponentially decaying energy density of axions, $\rho_a \propto e^{-t/\tau}$, leads to a logarithmic decrease in the maximum allowed τ given by the semi-analytic function

$$\tau_{\text{max}}(m_a) < \frac{4.3 \times 10^{-2}\,\text{s}}{1 + 0.25 \ln \frac{m_a}{2\,\text{GeV}}} \qquad (m_a \geq 2\,\text{GeV}). \tag{3.22}$$

Eq. (3.22) can also be written in terms of f_a by equating τ_{max}^{-1} with the analytic decay rate into gluons given by eqs. (3.3) and (3.4),

$$f_a \lesssim 1.2 \times 10^{10}\,\text{GeV} \left(\frac{m_a}{2\,\text{GeV}}\right)^{\frac{3}{2}} \left(\frac{\alpha_3}{0.3}\right) \left(\frac{1 + \frac{83}{4\pi}\alpha_3}{1 + \frac{83}{4\pi}0.3}\right)^{\frac{1}{2}} \left(1 + 0.25 \ln \frac{m_a}{2\,\text{GeV}}\right)^{-\frac{1}{2}} \qquad (m_a \geq 2\,\text{GeV}). \tag{3.23}$$

Thus, for $m_a \gg 2\,\text{GeV}$ and f_a small enough to be probed by accelerator experiments [45, 50, 60–68], the dark radiation constraint is absent.

4 Including a mirror photon

In this section we add a mirror photon γ' to the theory, with a mass sufficiently small that it can be ignored in our analysis. A mirror photon is natural in theories with a Z_2 symmetry that not only doubles the $\text{SU}(3)_c$ sector of the Standard Model to achieve a heavy QCD axion, but also doubles the $\text{SU}(2)_L \times \text{U}(1)_Y$ sector. This complete mirroring of the Standard Model gauge group introduces another axion coupling relevant in computing the amount of dark radiation

$$\mathcal{L}_{a,\gamma'} = \frac{g_{\gamma'}}{4} \frac{a}{f_a} F'_{\mu\nu} \tilde{F}'^{\mu\nu}. \tag{4.1}$$

JHEP04(2024)130

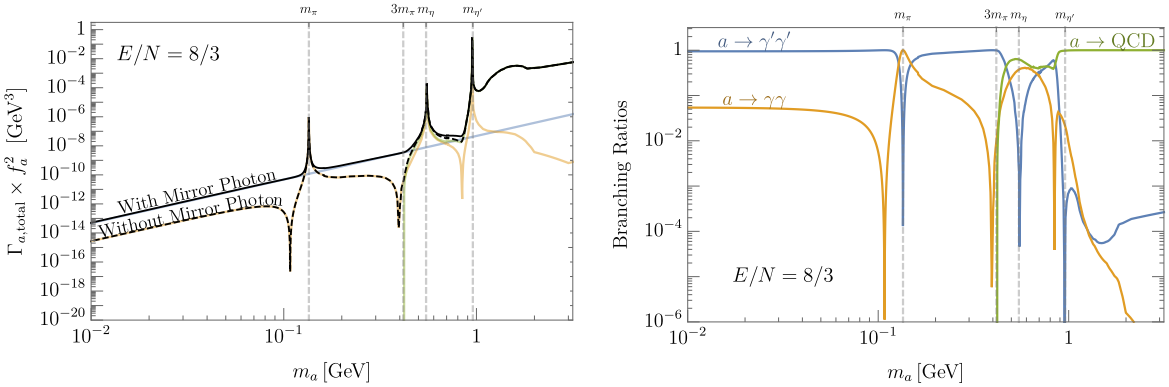

Figure 9. The axion total decay width (left) and branching ratios (right) as a function of axion mass, for $E/N = 8/3$. The orange (blue) contours refer to decays to photons (mirror photons); the green contour is for decays to states that include hadrons. In the left panel, the solid (dashed) black contours give the axion decay width in the theory with (without) mirror photons.

Above the mirror QCD scale, Λ'_{QCD}, the Z_2 symmetry ensures that

$$g_{\gamma'} = \frac{e'^2}{8\pi^2}\left(\frac{E}{N}\right), \tag{4.2}$$

with e' differing from e only by renormalization group scaling, which we ignore.

Note that unlike g_γ in (3.5), $g_{\gamma'}$ does not include contributions from axion-mirror meson mixing nor from the axial rotation onto mirror quarks because the masses of the lightest mirror quarks are typically much heavier than Λ'_{QCD} and thus irrelevant to the theory below Λ'_{QCD}. If, however, any mirror quark is lighter than the mirror QCD scale, then there is an additional contribution to $g_{\gamma'}$ analogous to the second and third terms in (2.13) for g_γ. In the minimal theory, where the Z_2 symmetry exchanges the Standard Model with its mirror and is spontaneously broken by a difference between the electroweak vevs with $v' \gg v$, all mirror quarks are heavier than Λ'_{QCD} for $f_a m_a \gtrsim 25\ \text{GeV}^2$ [69]. This relation is satisfied for nearly the entire parameter region of interest to us, so that all mirror quarks are well above the QCD scale; $g_{\gamma'}$ is thus uncorrected and given by (4.2).

Numerical results in this section are calculated taking $e' = e$ (that is, neglecting the small running of e' below v') and with a non-zero E/N so that g'_γ is non-zero. As a result, the axion-mirror photon decay rate is

$$\Gamma_{a\to\gamma'\gamma'} = \frac{g_{\gamma'}^2}{64\pi}\frac{m_a^3}{f_a^2} \simeq \frac{1}{64\pi}\left(\frac{e^2}{8\pi^2}\frac{E}{N}\right)^2\frac{m_a^3}{f_a^2}. \tag{4.3}$$

In particular, we consider three values for E/N: 8/3, motivated by grand unification, and 1/3 and 2/3, which can be achieved by an appropriate choice of KSVZ fermions. For example, $E/N = 2/3$ can be achieved by a KSVZ quark that possesses the same gauge quantum numbers as down quarks. For $E/N = 8/3$, the total axion decay rate with and without mirror photons is shown by the solid and dashed black contours in the left panel of figure 9. The light blue, orange, and green contours indicate the axion decay rates into γ', γ, and QCD degrees of freedom, respectively. Because there is no cancellation of terms in $g_{\gamma'}$ as

JHEP04(2024)130

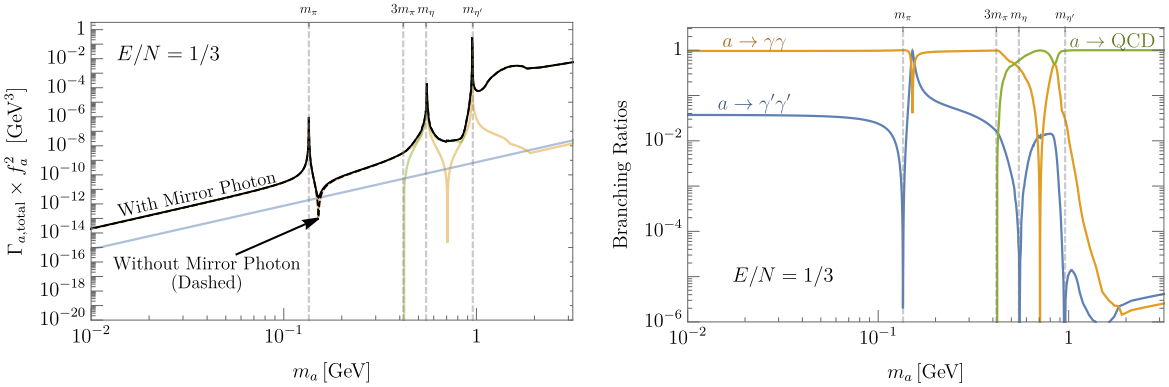

Figure 10. As in figure 9, but for $E/N = 1/3$. In the left panel, the solid and dashed black contours, giving the axion decay width with and without mirror photons, are almost conincident, as the partial width to mirror photons is sub-dominant, as shown by the straight blue line.

compared to g_γ, the $a \to \gamma'\gamma'$ decay rate (blue) is roughly an order of magnitude *greater* than the $a \to \gamma\gamma$ decay rate (orange) until $m_a \gtrsim 3m_\pi$: thus, axions below this mass dominantly decay into dark photons. This can be seen more clearly in the right panel of figure 9, which shows the branching ratios for the same three axion decay channels. The case for $E/N = 1/3$ is significantly different as demonstrated in figure 10. In particular, the cancellation between terms in g_γ is negligible which leaves the now smaller $a \to \gamma'\gamma'$ decay rate roughly an order of magnitude *weaker* than the $a \to \gamma\gamma$ decay rate.

We highlight these two representative values of E/N since they generate substantially different decay branching ratios into mirror photons.[2] This disparity is important since the parameter space where the axion branching ratio into dark photons is $\mathcal{O}(1)$ can be cosmologically dangerous as the mirror photon decay mode (4.3) increases N_{eff}, by directly generating dark radiation in the form of γ', and reduces the heating of the Standard Model bath as fewer axions decay into γ.

Quantitatively, N_{eff} with a mirror photon is

$$N_{\text{eff}} = \frac{8}{7}\left(\frac{11}{4}\right)^{4/3} \frac{\rho_\nu + \rho_{\gamma'}}{\rho_\gamma}\,, \tag{4.4}$$

where ρ_ν, $\rho_{\gamma'}$, and ρ_γ, are the relic energy densities of neutrinos, mirror photons, and photons, respectively. According to eq. (4.4), an additional mirror photon in thermal equilibrium significantly increases N_{eff} and is generally excluded by current ΔN_{eff} limits [19]. Nevertheless, a mirror photon can be allowed if it does not achieve a thermal abundance.

This leads us to consider the Boltzmann equation for $f_a(\mathbf{p})$ in the freeze-in picture

$$\frac{\partial f_a}{\partial t} - p_a H \frac{\partial f_a}{\partial p_a} = (C_\gamma + C_P + C_\pi + C_\Gamma)(f_{a,\text{eq}} - f_a) - C_{\gamma'} f_a\,, \tag{4.5}$$

where the mirror photon collision term, $C_{\gamma'}$, is given by

$$C_{\gamma'} \simeq \frac{m_a}{E_a}\Gamma_{a\to\gamma'\gamma'}\,. \tag{4.6}$$

[2]The case for $E/N = 2/3$ is intermediate between these two cases and like the case $E/N = 1/3$, also yields a region of $\Delta N_{\text{eff}} \approx 0$ at low m_a.

JHEP04(2024)130

Eq. (4.5) replaces eq. (3.8) when including mirror photons. In addition, while the energy density evolution of the Standard Model bath remains as given in eqs. (3.17) and (3.19),[3] the energy density evolution of γ' is described by

$$\frac{\partial \rho_{\gamma'}}{\partial t} + 4H\rho'_{\gamma} = \int \frac{d^3p}{(2\pi)^3} m_a \Gamma_{a\to\gamma'\gamma'} f_a = m_a \Gamma_{a\to\gamma'\gamma'}\, n_a\,. \tag{4.7}$$

Conservatively, we take the initial γ' density at $T_{\chi\mathrm{PT}}$ to be zero. Due to the substantial change in Standard Model degrees of freedom across T_{QCD}, freeze-in production of γ' much earlier than $T_{\chi\mathrm{PT}}$ is diluted and this conservative estimate is a fairly good approximation to the true initial abundance of γ'. Last, the Hubble expansion rate, (3.21), is modified to include the additional mirror photon energy density,

$$H^2 = \left(\frac{\dot{R}}{R}\right)^2 = \frac{8\pi G}{3}\left(\rho_\gamma + \rho_e + \rho_\mu + \rho_\pi + \rho_{\delta_{\mathrm{QCD}}} + \rho_{\nu_e} + \rho_{\nu_{\mu\tau}} + \rho_a + \rho_{\gamma'}\right). \tag{4.8}$$

Figures 11, 12, and 13 show the contours of N_{eff} when including a massless mirror photon in heavy axion cosmologies for $E/N = 8/3$, $1/3$, and $2/3$, respectively. As before, the blue region indicates where N_{eff} is excluded by current CMB measurements at the 2σ level. Note that whereas ΔN_{eff} is strictly negative in the case without the mirror photon (figures 6 and 7), the case with the mirror photon gives positive ΔN_{eff} for most of the parameter space where the mirror photon dominates the branching ratio.

The green region indicates where the mirror photon reaches equilibrium and the freeze-in picture breaks down. This occurs when $\Gamma_{a\gamma'\gamma'} \gtrsim H(T = m_a)$, or equivalently, roughly when

$$f_a \lesssim 10^5\,\mathrm{GeV}\left(\frac{m_a}{125\,\mathrm{MeV}}\right)^{\frac{1}{2}}\left(\frac{E/N}{8/3}\right). \qquad \text{(Mirror Photon reaches thermal equil.)} \tag{4.9}$$

Within this green region, the contour values for N_{eff} are artificially high because the mirror photon acquires a greater than thermal abundance due to the lack of a back reaction in eq. (4.5). In principle, capping the mirror photon abundance at a thermal abundance suggests that realistic N_{eff} contours within the green region are roughly fixed at the value of N_{eff} on the boundary of the green region; that is, the value of N_{eff} when the mirror photon *just* acquires a thermal abundance from the freeze-in picture. For axions decaying prior to neutrino decoupling, this argument suggests $N_{\mathrm{eff}} \gtrsim 3.8$ in the green region when $E/N = 8/3$. Such a large ΔN_{eff} is already excluded by experiments and thus the freeze-in picture is generally valid within the experimentally allowed region. However, for axions decaying after neutrino decoupling, it is possible that a tuned cancellation between the $\rho_{\gamma'}$ energy deposit (positive ΔN_{eff} contribution) and the heating of ρ_γ relative to neutrinos (negative ΔN_{eff} contribution) can occur in the green region. We leave the calculation of such a tuned cancellation to future

[3]The axion-mediated interaction $\gamma' + \gamma' \leftrightarrow \gamma + \gamma$ can contribute to the energy transfer to the Standard Model thermal bath and hence to additional terms on the right-hand-side of Eq. (3.17). However, this interaction is $\mathcal{O}(1/f_a^4)$ and generally negligible. Similarly, the decay and inverse decay $a \leftrightarrow \gamma + \gamma'$ can also modify (3.17), but this requires $O(1)$ kinetic mixing or $aF'\tilde{F}$. The former is constrained by searches for relic mirror charged particle [70], and the latter requires $\mathrm{U}(1) \times \mathrm{U}(1)'$ charged particles around the mass scale f_a, whose relic is also constrained.

JHEP04(2024)130

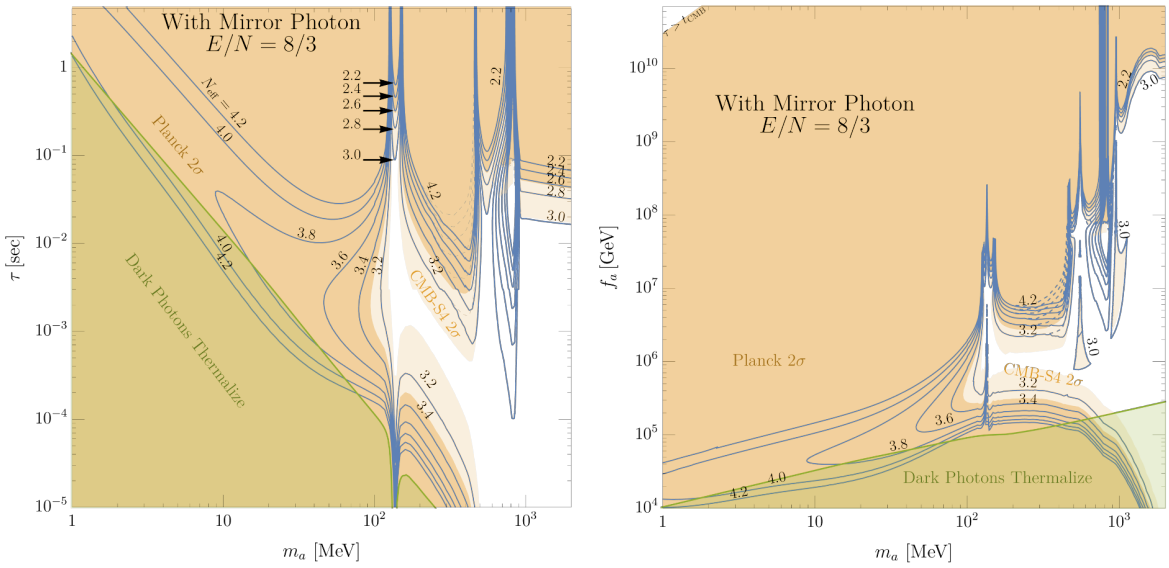

Figure 11. Contours of $N_{\rm eff}$ in the $m_a - \tau$ (left) and $m_a - f_a$ (right) planes for $E/N = 8/3$ when including a mirror photon. The dashed contours indicate where the initial axion yield is uncertain because $T_{\rm FO}$ lies between $T_{\chi \rm PT}$ and $T_{\rm gPT}$. The dashed contours bound this uncertainty by showing the value of $N_{\rm eff}$ taking the minimum initial axion yield while the solid contours show the value of $N_{\rm eff}$ taking the maximum initial axion yield as given in figure 2. The green region shows where f_a is sufficiently small that the dark photon reaches a thermal abundance and the freeze-in picture we employ breaks down. The dark orange region is excluded at 95% confidence by Planck, while the light orange shows the future reach of CMB-S4 experiment at 95% confidence.

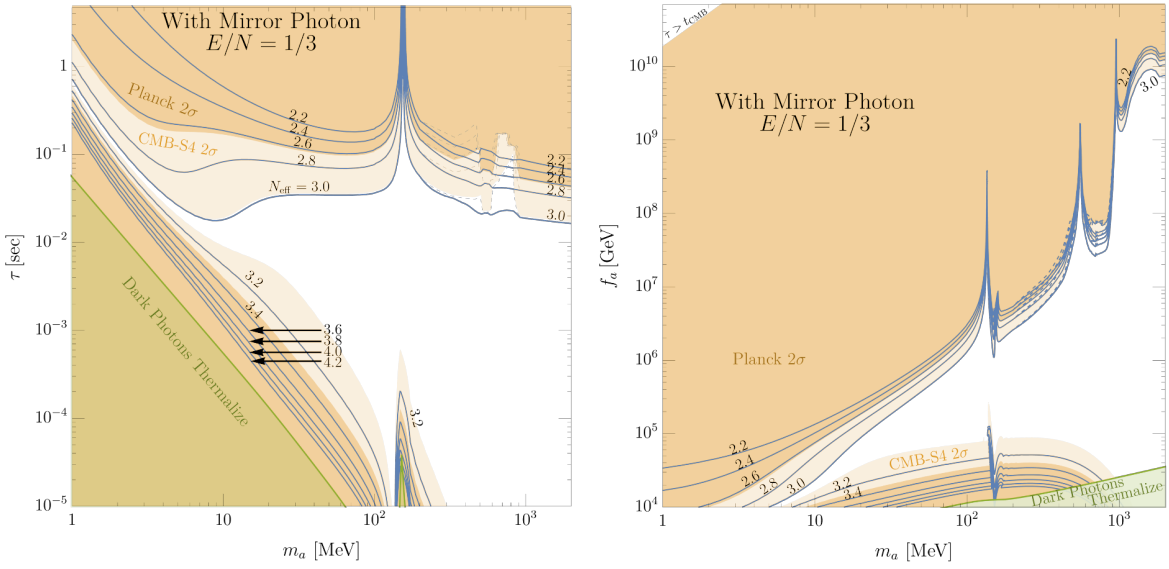

Figure 12. Same as figure 11, but for $E/N = 1/3$.

JHEP04(2024)130

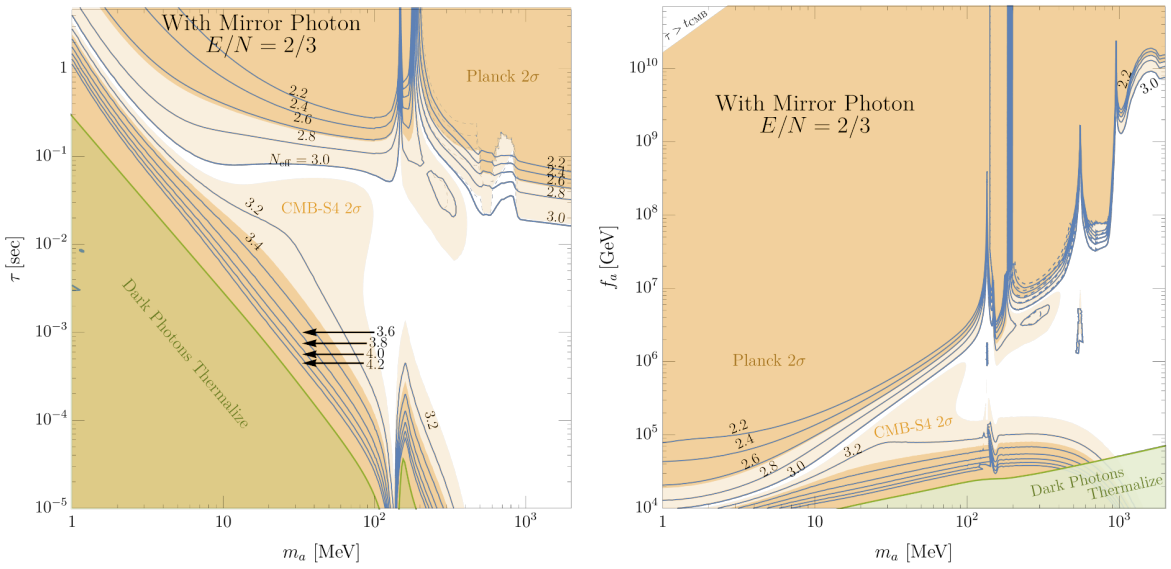

Figure 13. Same as figure 11, but for $E/N = 2/3$.

work, but we expect that the parameter region with $\tau \gtrsim 1$ sec is excluded by BBN. This is because to cancel the positive $\Delta N_{\rm eff}$, the axion decays before the proton-neutron conversion completes, and the Helium abundance will be affected.

5 Light axion and dark matter over-production

In this section, we discuss constraints on the heavy QCD axion for $m_a < 1\,\text{MeV}$. As its mass is decreased the axion remains excluded by $\Delta N_{\rm eff}$ until it decays after the CMB era. However, at this point, the axions remains excluded from its contribution to dark matter at the CMB era, until a significant further reduction in its mass. Before entering the allowed light axion region, there is an excluded region from free-streaming effects on large scale structure.

As can be seen from figure 6 and 7, the CMB limit on $\Delta N_{\rm eff}$ excludes $1\,\text{MeV} \lesssim m_a \lesssim 3\,\text{MeV}$ for any f_a. This exclusion from $\Delta N_{\rm eff}$ continues for $m_a < 1\,\text{MeV}$, until the axions decay after recombination.[4] Hence, the blue region of figure 14, where $\tau < t_{\rm CMB} \equiv 370,000$ yrs ($z \approx 1100$) [51], is excluded by $\Delta N_{\rm eff}$. For $\tau \gtrsim t_{\rm CMB}$ and $m_a > 0.13(\Omega_{\rm DM}h^2/0.12)Y_a(T_{\rm FO,g})^{-1}\,\text{eV}$, the axion is sufficiently heavy and long-lived to exceed the observed dark matter density at the CMB era, as shown by the excluded orange region of figure 14. Here, we assume the reheat temperature is sufficiently high that axions undergo freeze-out, as shown in figure 1, giving an axion freeze-out yield, $Y_a(T_{\rm FO,g})$, typically between 2×10^{-3} to 2×10^{-2}. Relaxing this assumption, by taking $T_{\rm RH}$ below $T_{\rm FO,g}$ or by introducing dilution between axion freeze-out and BBN, reduces the orange excluded region.

At lower axion masses, the free-streaming of axions suppresses the matter spectrum (i.e., the axion is hot dark matter) and for even smaller masses, the axion works as dark radiation. We reinterpret the bound derived in [71] for our framework and exclude the green-shaded

[4]The parameter space where the axions decay before recombination but are in thermal equilibrium at BBN and generate a positive $\Delta N_{\rm eff}$ is discussed in [26, 27, 52], but is weaker than the bounds in this work.

JHEP04(2024)130

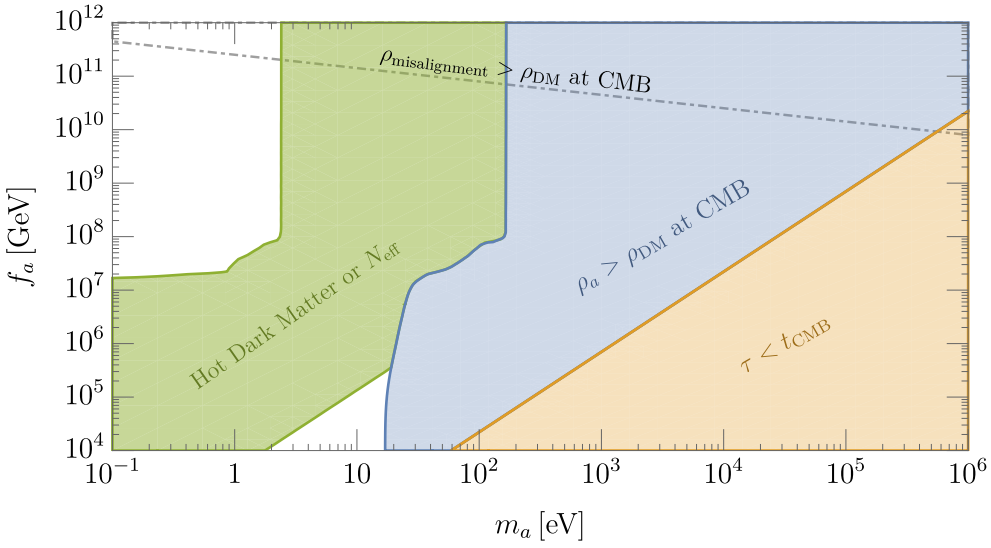

Figure 14. Cosmological constraints on the low mass axion region, $m_a < 1\,\text{MeV}$. The axion decays prior to recombination ($t_{\rm CMB} \approx 370,000$ yr) in the orange region, which is excluded by the $N_{\rm eff}$ constraint. The boundary denoting $\tau = t_{\rm CMB}$ is given for $E/N = 0$ (solid) and 8/3 (dashed) without a mirror photon; and for 1/3 (dotted) and 8/3 (dot-dashed) with a mirror photon decay channel. In the blue region, the axion decays after recombination, but possesses a matter energy density during the CMB era exceeding that measured by Planck [19], assuming the axion froze-out in the early Universe. For $f_a \lesssim 10^8\,\text{GeV}$, $T_{\rm FO}$ occurs below the electroweak scale, and hence the axion energy density at $t_{\rm CMB}$ grows because of the reduction in g_*. In the green region, the axion suppresses the structure formation as hot dark matter or contributes to dark radiation.

region in figure 14. Here we conservatively impose the bound only for $\tau > t_0$, where t_0 is the present age of the Universe, but we expect that the bound is also applicable as long as $\tau > t_{\rm eq}$, since the suppression of the matter spectrum is dominated by the free-streaming of axions before the matter-radiation equality. A part of orange, blue, or green region is also excluded by other astrophysical constraints (see [72] for an overview), but they are generically weaker.

Finally, the misalignment mechanism [73–75] overproduces axion dark matter above the dotted-dashed line in figure 14. Here we assume an $O(1)$ misalignment angle.

6 Conclusions

The strong CP problem can be addressed in a wide variety of axion models. The minimal ones, where the QCD axion mass is solely given by strong QCD dynamics, predict $m_a f_a \sim (100\,\text{MeV})^2$, but are typically plagued by a quality problem. This quality problem can be ameliorated or solved in a range of "Heavy QCD Axion" theories, where $m_a f_a$ is orders of magnitude larger than in the minimal models. The constraints and search strategies for these heavy axions are completely different from those for the conventional lighter axion. An important constraint from CMB data arises if the axion lifetime is in the range of $10^{-1}\,\text{s}$ – $10^{-12}\,\text{s}$, decaying after neutrino decoupling at the MeV era, but before last scattering of the CMB at the eV era. In this case, the energy density of neutrinos is diluted, affecting the dark radiation at the CMB era, $N_{\rm eff}$, which has been precisely measured by the Planck

JHEP04(2024)130

Collaboration [19] and will be significantly improved by CMB Stage 4 experiments [20]. Thus, theory and experiment both strongly motivate a detailed study of this cosmological bound on heavy axions. For axion masses above 1 MeV, except for accelerator searches at low values of f_a, $N_{\rm eff}$ is the strongest bound on the heavy QCD axion, and is the focus of this work.

A well-motivated and predictive model involves a mirror copy of the SM with a large axion mass generated by the mirror QCD interaction. In this case there is a competition between axion decays to photons diluting the neutrino contribution to $N_{\rm eff}$ and axion decays to mirror photons directly enhancing $N_{\rm eff}$. We have also provided a detailed analysis of the $N_{\rm eff}$ bound in theories with a light mirror photon.

Our analysis of the $N_{\rm eff}$ bound takes into account key pieces missing from previous studies of the heavy QCD axion by developing a Boltzmann code that follows the evolution of the momentum distribution for the axion. The mesons and gluons of QCD play a key role; we include axion-pion scattering, axion decay to final states involving mesons, and axion-meson mixing. In addition we follow a detailed cosmological evolution from the initial axion abundance from freeze-out to the non-trivial QCD contributions in the Friedmann equations.

Our results for the CMB $N_{\rm eff}$ constraints on the heavy QCD axion, in the absence of a mirror photon, are shown in figures 6 and 7, and are very powerful. Planck excludes large areas of parameter space, especially at large f_a , but large areas remain at low f_a, where the quality problem is solved for operators of dimension 6 and larger. The discovery reach of CMB-S4 at larger values of m_a is modest, but improves at lower m_a: for example, if f_a is of order 10^4 GeV, CMB-S4 will see a signal for m_a in the range of (3-10) MeV.

We find two important differences from standard results, illustrated by comparing figure 5 with our results shown in figures 6 and 7. First, resonances occur when the axion mass is around the π_0, η, and η' masses, greatly affecting $N_{\rm eff}$ for axion masses between $(100 - 1000)$ MeV. Second, by including mesons and gluons, we correctly take account of the axion lifetime. This is a large effect, especially at large m_a, increasing the decay rate by orders of magnitude as m_a rises above ~ 1 GeV; this point is apparent in the right panels of figures 6 and 7 where regions with higher f_a open up.

In the presence of a light mirror photon, our results for the CMB $N_{\rm eff}$ constraints are shown in figures 11, 12, and 13 for $E/N = 8/3$, $1/3$, and $2/3$ respectively. For $E/N = 8/3$, $m_a < 100$ MeV is excluded for all values of f_a. A substantial fraction of the allowed region with 100 MeV $< m_a <$ 500 MeV will be probed by CMB-S4 via a positive signal for $\Delta N_{\rm eff}$. For $E/N = 1/3$, the CMB $N_{\rm eff}$ bound is considerably weaker. A new allowed region opens up at lower axion masses, 1 MeV $< m_a <$ 100 MeV, where dark radiation from the mirror photon compensates neutrino dilution from axion decays. A large fraction of this region gives a CMB-S4 signal, with $\Delta N_{\rm eff}$ positive (negative) for smaller (larger) values of f_a. Finally, the $N_{\rm eff}$ bound in the $E/N = 2/3$ case is also weaker than the $E/N = 8/3$ case, but not as weak as compared to $E/N = 1/3$. These allowed regions both solve the quality problem for operators of dimension 6 and larger.

The current and future 95% confidence limit on the axion mass from $N_{\rm eff}$ in this work are shown in comparison to other cosmological and astrophysical constraints in figure 15. The limits on $N_{\rm eff}$ in this work provide the strongest constraints on heavy QCD axions for $m_a \gtrsim 1$ MeV and $f_a \gtrsim 10^5$ GeV. Complementary constraints at small f_a arise from

JHEP04(2024)130

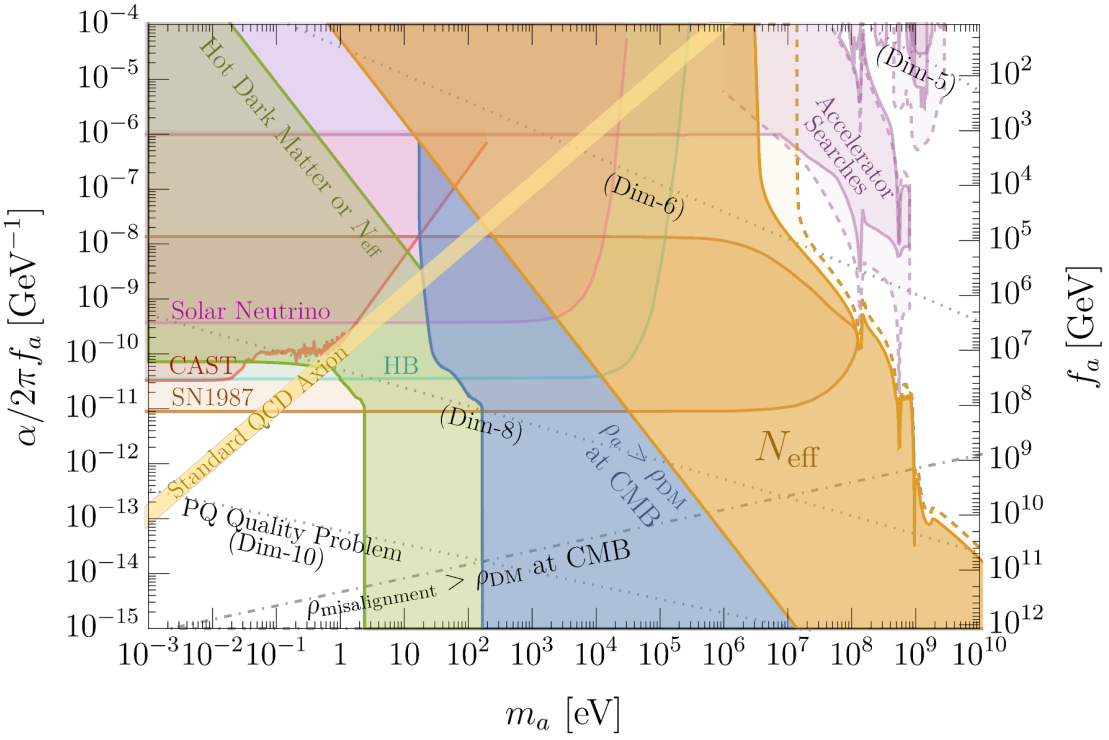

Figure 15. Overview of the excluded parameter space as determined in this work (blue region) in relationship to other QCD axion bounds. The solid orange region shows the 2σ exclusion region on $N_{\rm eff}$ as determined by Planck for the heavy QCD axion with $E/N = 0$ (see figure 6). The dashed orange contour shows the future reach of $N_{\rm eff}$ from CMB-S4. The left boundary of the orange region indicates where the axion decays after recombination which marks the parameter space where $N_{\rm eff}$ contstraints become inapplicable (see figure 14). The blue region indicates where the axion energy density at recombination is greater than that of dark matter, assuming the reheat temperature of the universe is high enough that the axion froze-out with a thermal abundance. The solid and dashed purple regions shows the present and future bounds from accelerator searches, respectively [45, 50, 60–68]. The brown region shows the bound from supernova 1987a on axions with hadronic interactions, [76], green from horizontal-branch cooling [77], red from CAST [78, 79], and pink from solar neutrinos [80]. Below the dot-dashed contour, the axion energy density arising from the misalignment mechanism, with a misalignment angle of unity, is greater than the observed dark matter energy density. In the green region, the axion suppresses the structure formation or contributes to $N_{\rm eff}$. Below the dotted contours, the axions suffers a PQ quality problem arising from operators of the labeled dimension. The diagonal yellow strip indicates the standard QCD axion, which highlights the severity of the PQ quality problem for low mass axions.

direct heavy axion searches at accelerators [45, 68] as shown by the purple shaded regions. Producing axions in a beam dump, such as the DUNE Near Detector, and discovering their subsequent decays, will allow the region enclosed by the dashed purple contour to be probed [45]. Furthermore, the dashed purple contour at higher m_a and low f_a can be probed by observing axions in B meson decays at Belle [68]. The bound from axion cooling of Supernova 1987A has uncertainties arising from the temperature and density profiles of the supernova, and has been computed for a variety of such profiles in [76]; we show a

JHEP04(2024)130

conservative case. Constraints on the decay of the axion from extragalactic background light or CMB spectral distortions are derived in [18], but the constraints do not exclude the parameter region that is allowed in figure 15.

The bounds shown in figure 15, and elsewhere in the paper, are computed assuming that the reheat temperature of the universe $T_{\rm RH}$ is above the axion freeze-out temperature, and that there is no subsequent dilution of the axion abundance, for example from late decaying particles. Removing this assumption relaxes the bounds, since axion production occurs via freeze-in rather than freeze-out, or is diluted after freeze-out. Since the freeze-out temperature decreases as f_a drops, relaxing the bounds becomes harder at lower f_a. For $f_a < 10^4\,\text{GeV}$, the axion is kept into thermal equilibrium even at $T < 4\,\text{MeV}$, and the BBN bound $T_{\rm RH} > 4\,\text{MeV}$ [81–83] excludes the possibility of relaxing the bound. It may be plausible that the reheating temperature is below the freeze-out temperature for large f_a, but solving the quality problem favors low f_a, and it is typically harder to obtain a large enough m_a for large f_a; see e.g., eq. (1.3).

The next decade will yield exciting and important answers to axion physics. Heavy QCD axions provide a highly-motivated solution to the strong CP problem. Unlike the standard QCD axion, which induces a small $\Delta N_{\rm eff}$ signal [26], heavy QCD axions can generate substantial $\Delta N_{\rm eff}$ signals that can be probed by the exquisite sensitivity of current and near future CMB telescopes. Moreover, in theories without a mirror photon, this signal results from a *depletion* of the cosmic neutrino abundance, providing a less common fingerprint of a *negative* contribution to $\Delta N_{\rm eff}$. Such a measurement would determine a correlation between the axion mass and decay constant.

Acknowledgments

We thank Jeffrey Anderson, Raymond Co, and Jonathan Wurtele for providing useful computational resources. We also thank Tobioka Kohsaku, Takemichi Okui, Taeyhun Jung, and Jiabao Wang for pointing out typos. This work was supported in part by the Director, Office of Science, Office of High Energy and Nuclear Physics, of the US Department of Energy under Contracts DE-AC02-05CH11231 (LJH) and by the National Science Foundation under grant PHY-1915314 (LJH).

A Calculation of axion-pion collision term

In this section, we compute the axion-pion scattering collision term, C_π, used in the axion-Boltzmann equation, (3.17). The interaction between an axion, neutral pion, and two charged pions includes the following three interactions, $a(p_a) + \pi_0(p_1) \leftrightarrow \pi_+(p_2) + \pi_-(p_3)$, $a(p_a)+\pi_-(p_1) \leftrightarrow \pi_0(p_2)+\pi_-(p_3)$, and $a(p_a)+\pi_+(p_1) \leftrightarrow \pi_+(p_2)+\pi_0(p_3)$ as shown in figure 16. According to the chiral Lagrangian (2.2), the matrix element for $a + \pi_0 \to \pi_+ + \pi_-$ is

$$\mathcal{M}_{a+\pi_0\to\pi_++\pi_-} = \frac{3}{2}\frac{A}{f_a f_\pi}\frac{1}{1-r^2}(s - m_\pi^2), \tag{A.1}$$

where $s = (p_a + p_1)^2$. The matrix elements for $a + \pi_- \to \pi_- + \pi_0$ and $a + \pi_+ \to \pi_+ + \pi_0$ scattering are obtained by the four momentum mapping $p_1 \to -p_2$ and $p_1 \to -p_3$, respectively.

JHEP04(2024)130

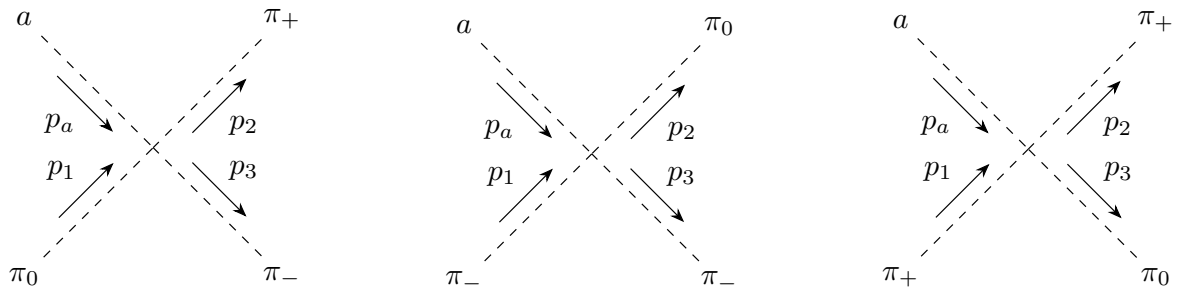

Figure 16. Feynman diagrams associated with axion-pion scattering involving charged pions.

As a result, the total squared amplitude for scatterings involving the axion and charged pions is

$$\begin{aligned} |\mathcal{M}|^2_{a+\pi_i\to\pi_j^\dagger+\pi_k^\dagger} &= |\mathcal{M}|^2_{a+\pi_0\to\pi_++\pi_-} + |\mathcal{M}|^2_{a+\pi_-\to\pi_-+\pi_0} + |\mathcal{M}|^2_{a+\pi_+\to\pi_++\pi_0} \\ &= \left(\frac{3}{2}\frac{A}{f_a f_\pi}\frac{1}{1-r^2}\right)^2 \left[(s-m_\pi^2)^2 + (t-m_\pi^2)^2 + (u-m_\pi^2)^2\right] \\ &= \left(\frac{3}{2}\frac{A}{f_a f_\pi}\frac{1}{1-r^2}\right)^2 \left[s^2+t^2+u^2-3m_\pi^4-2m_a^2m_\pi^2\right], \end{aligned} \tag{A.2}$$

where $t \equiv (p_a - p_2)^2$, $u \equiv (p_a - p_3)^2$ and π_i, π_j, π_k in the subscript of (A.2) refer to three pions of different charge π_0, π_+, π_-. Likewise, the interaction between an axion and three neutral pions generates the squared scattering amplitude

$$|\mathcal{M}|^2_{a+\pi_0\to\pi_0+\pi_0} = \left(\frac{3}{2}\frac{A}{f_a f_\pi}\frac{1}{1-r^2}\right)^2 m_a^4. \tag{A.3}$$

Inserting the sum of the squared scattering matrix elements, (A.2) and (A.3), into eq. (3.9) and integrating over the phase spaces of the three pions gives the product of the axion-pion collision term and $f_{a,\mathrm{eq}} - f_a$

$$\begin{aligned} C_\pi(f_{a,\mathrm{eq}} - f_a) = \frac{1}{2E_a}\int \Big[d\Pi_1\, d\Pi_2\, d\Pi_3 (|\mathcal{M}|^2_{a+\pi_i\to\pi_j^\dagger+\pi_k^\dagger} + \frac{1}{2!}|\mathcal{M}|^2_{a+\pi_0\to\pi_0+\pi_0}) \\ \times \Lambda (2\pi)^4 \delta^4(p_a + p_1 - p_2 - p_3)\Big], \end{aligned} \tag{A.4}$$

where

$$\Lambda = (1+f_a)(1+f_1) f_2 f_3 - f_a f_1 (1+f_2)(1+f_3) \tag{A.5}$$

$$\simeq (f_{a,\mathrm{eq}} - f_a) f_1 (1 + f_2 + f_3)\,, \tag{A.6}$$

and f_i is the distribution function of particle i possessing momentum p_i in accordance with figure 16. In going from (A.5) to (A.6), we take the pions to be in thermal equilibrium with the Standard Model thermal bath so that f_1, f_2, and f_3 follow a Bose-Einstein distribution of temperature T. The temperature T of the strongly coupled thermal bath is inferred at each numerical time step by solving the following equation for T:

$$\sum_{i=\gamma,e,\mu,\pi,\delta_{\mathrm{QCD}}} \rho_i = \rho_\gamma(T) + \rho_e(T) + \rho_\mu(T) + \rho_\pi(T) + \rho_{\delta\mathrm{QCD}}(T) \tag{A.7}$$

JHEP04(2024)130

where the left-hand side of (A.7) is solved from eq. (3.17) and the right-hand side is calculated from eq. 3.18 for γ, μ, e, π and from [58] for $\rho_{\delta_{\rm QCD}}$, as described more in appendix C.

To calculate C_π, we first introduce another δ-function in (A.4) by writing $d\Pi_3(2\pi)^3 = \frac{d^3\mathbf{p}_3}{2E_3} = d^4p_3\delta(p_3^2-m_3^2)\Theta(p_3^0)$. By integrating p_3 over the other delta function $\delta^4(p_a+p_1-p_2-p_3)$, eq. (A.4) simplifies to

$$C_\pi(f_{a,\rm eq}-f_a) = \frac{1}{2E_a}\int\Big[d\Pi_1\, d\Pi_2(|\mathcal{M}|^2_{a+\pi_i\to\pi_j^\dagger+\pi_k^\dagger}+\frac{1}{2!}|\mathcal{M}|^2_{a+\pi_0\to\pi_0+\pi_0})\Lambda 2\pi\delta(p_3^2-m_3^2)\Theta(p_3^0)\Big], \tag{A.8}$$

with the understanding that $p_3 = p_a + p_1 - p_2$. Note that the argument of the remaining delta-function, $p_3^2 - m_3^2$, can be written as

$$Q + 2\left((E_aE_1 - |\mathbf{p}_a||\mathbf{p}_1|\cos\alpha) - (E_1E_2 - |\mathbf{p}_1||\mathbf{p}_2|\cos\gamma) - (E_aE_2 - |\mathbf{p}_a||\mathbf{p}_2|\cos\theta)\right) \tag{A.9}$$

where, in the notation of [84], $Q = -m_3^2 + m_a^2 + m_1^2 + m_2^2$, and α, θ, γ are the angles between $\mathbf{p}_a$ and $\mathbf{p}_1$, $\mathbf{p}_a$ and $\mathbf{p}_2$, and $\mathbf{p}_1$ and $\mathbf{p}_2$, respectively. It is convenient to express the latter angle in terms of the former two by $\cos\gamma = \cos\alpha\cos\theta + \sin\alpha\sin\theta\cos\beta$.

In the massless axion limit, the argument of the remaining delta function can easily be expressed in terms of E_a as done in [53]. However, in the massive axion limit, this is impossible and it is thus more useful to move the argument of the delta function onto one of the scattering angles, as done in [84], which we follow. In particular, the choice of the angle β is most convenient as it only occurs once in (A.9). The resulting integral for C_π is

$$\begin{aligned} C_\pi(f_{a,\rm eq}-f_a) = \frac{1}{2E_a}\int\Big[&\left(\frac{d|\mathbf{p}_1|}{(2\pi)^3}\frac{\mathbf{p}_1^2}{2E_1}d\cos\alpha\, d\beta\right)\left(\frac{d|\mathbf{p}_2|}{(2\pi)^3}\frac{\mathbf{p}_2^2}{2E_2}d\cos\theta\, d\phi\right) \\ &\times(|\mathcal{M}|^2_{a+\pi_i\to\pi_j^\dagger+\pi_k^\dagger}+\frac{1}{2!}|\mathcal{M}|^2_{a+\pi_0\to\pi_0+\pi_0})\Lambda\left(\sum_{\beta_i}\frac{2\pi\delta(g(\beta))}{\left|\frac{dg}{d\beta}\right|_{\beta=\beta_i}}\right)\Theta(p_3^0)\Big] \end{aligned} \tag{A.10}$$

where $g(\beta) = p_3(\beta)^2 - m_3^2$. The integrals over the azimuthal angles β and ϕ can be done analytically due to the delta function and the lack of ϕ dependence in the integrand. The remaining integrals over the pion 3-momenta $|\mathbf{p}_1| \in [0,\infty)$ and $|\mathbf{p}_2| \in [0,\infty)$ and the polar angles $\cos\alpha \in [-1,1]$ and $\cos\theta \in [-1,1]$ are done numerically using Monte Carlo integration. To ensure the integration region is performed only in the kinematically allowed region, we include a Heaviside function $\Theta(1-\cos^2\beta_i)$ in (A.10), where β_i is the location of the two (equal and opposite) roots of $g(\beta)$ [84]. Note that β_i are functions of the other four integration variables.

We can gain intuition for the cosmological effect of axion-pion scattering by calculating the thermally averaged pion-to-axion scattering rate as introduced in eq. (3.2),

$$\Gamma_{a\pi\leftrightarrow\pi\pi} = \frac{1}{n_{a,\rm eq}}\int\frac{d^3\mathbf{p}_a}{(2\pi)^3}\mathcal{C}_\pi f_{a,\rm eq} \equiv \frac{T^5}{f_a^2 f_\pi^2}\frac{A^2}{(1-r^2)^2}\mathcal{F}_\pi(m_a,T), \tag{A.11}$$

where $n_{a,\rm eq}$ is the thermal number density of axions with mass m_a at temperature T. As before, $A \equiv \frac{1}{3}(1-z)/(1+z)$, $z \equiv m_u/m_d$, and $r \equiv m_a/m_\pi$. Figure 17 shows $\mathcal{F}_\pi$ as a function

JHEP04(2024)130

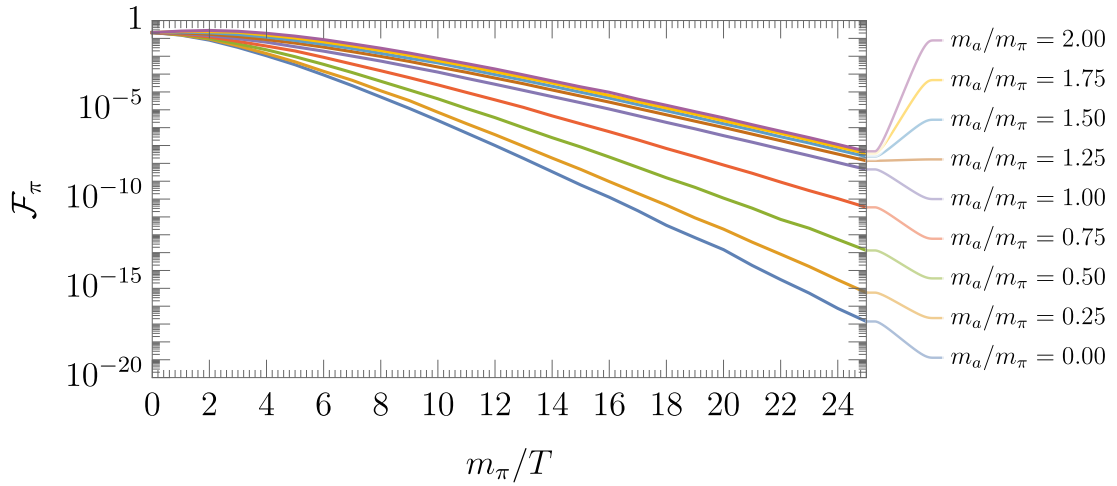

Figure 17. Numerical evaluation of $\mathcal{F}_\pi$ as a function of m_π/T for a variety of axion masses. $\mathcal{F}_\pi$ becomes suppressed for $m_a > m_\pi$ and $T < m_\pi$ since the production of axions must occur at the Boltzmann tail of the incoming pions. The massless axion limit, which has been computed previously in literature [53, 57], corresponds to the $m_a/m_\pi = 0$ contour.

of m_π/T for a variety of axion masses. For $m_a \ll m_\pi$, $\mathcal{F}_\pi$ reduces to previous results in the literature for massless axions [53, 57], with $\mathcal{F}_\pi$ related to the $h_{\rm LO}$ function defined in [53, 57] by the mapping $\mathcal{F}_\pi(m_\pi/T, m_a = 0) \equiv 0.212\, h_{\rm LO}(m_\pi/T)$. According to figure 17, for $T < m_\pi$, $\mathcal{F}_\pi$ drops as m_a increases. This is because in this regime, only the Boltzmann tail of pions with high energies m_a can kinematically scatter to produce axions.

B $N_{\rm eff}$ for large axion masses

In the main text, we show the $N_{\rm eff}$ constraint for $m_a < 2\,\text{GeV}$. In this appendix, we derive the constraint for $m_a > 2\,\text{GeV}$.

In the left panels of figure 6, 7, 11 and 12, the $N_{\rm eff}$ contours become approximately horizontal above $m_a \approx 1\,\text{GeV}$, signifying that $N_{\rm eff}$ is dictated mainly by the lifetime of the axion in this region. However, careful inspection indicates that the slope of the contours is not quite flat, but slightly decreases as m_a grows. The reason is, for fixed τ, the energy density of the axion at decay increases with increasing mass. This follows because axions in this region have such large f_a that they decouple early and decay non-relativistically. Thus, what actually sets the $N_{\rm eff}$ contours in the $m_a > 2\,\text{GeV}$ region is how much energy density they deposit into the thermal bath right at neutrino decoupling.

For example, let $\rho_{\rm max}$ be the maximum energy density that can be deposited at a certain time t_* so that $N_{\rm eff}$ does not drop below an arbitrary contour, $N_{\rm eff,0}$, which we will take to be $\simeq 2.62$, the 2σ limit on $N_{\rm eff}$ allowed by Planck. Choose a point (m_0, τ_0) that lies on this $N_{\rm eff,0}$ contour in the $m_a \gtrsim 1\,\text{GeV}$ region. Analytically, the energy density of this non-relativistic axion at time t_* is

$$\rho(t_*) = \rho_{\rm init}\left(\frac{a_{\rm init}}{a(t_*)}\right)^3 e^{-t_*/\tau_0} = m_0 Y_0 s(t_*) e^{-t_*/\tau_0} \equiv \rho_{\rm max} \tag{B.1}$$

JHEP04(2024)130

where Y_0 is the axion yield, and $s(t_*)$ the entropy density at time t_*. Note eq. (B.1) defines $\rho_{\max}$. It follows that for axions of different (m_a, τ) to possess the same energy density as $\rho_{\max}$ at time t_*, requires

$$\frac{m_0 Y_0}{m_a Y_a} = \exp t_* \left(\frac{1}{\tau_0} - \frac{1}{\tau} \right) \tag{B.2}$$

or equivalently,

$$\tau = \frac{\tau_0}{1 + \frac{\tau_0}{t_*} \ln \left(\frac{m_a Y_a}{m_0 Y_0} \right)}, \tag{B.3}$$

We perform a numerical fit of the $N_{\text{eff},0} = 2.62$ contour with the anchor point $(m_0, \tau_0) = (2.0\,\text{GeV}, 4.3 \times 10^{-2}\,\text{s})$ and find $t_* \simeq 0.17\,\text{s}$. Other anchor points give similar t_*. Eq. (3.22) follows from this fit.

C Numerical approaches

In this section, we discuss the numerical techniques used to solve the Boltzmann equation describing the cosmological evolution of the axion. As mentioned in section 3.2, we employ the method of lines technique to convert the Boltzmann system of partial differential equations into a system of ordinary differential equations. In particular, we discretize the partial differential equation governing the axion phase space density, (3.8), into a partition of N ordinary differential equations, $\{f_{\tilde{\mathbf{p}},\mathbf{i}}(t)\}$ of time, with each ODE corresponding to the time evolution of the phase space density at a fixed comoving momentum, $|\tilde{\mathbf{p}}_i| = |\mathbf{p}_i| a(t)$, with $i \in \{1, \ldots, N\}$. In our numerical setup, we split (3.8) into $N = 24$ ODEs of logarithmically equidistant $|\tilde{\mathbf{p}}_i|$ where $i = 1$ corresponds to the fixed comoving momentum $|\tilde{\mathbf{p}}_1| = e^{-8} T_{\chi\text{PT}}$ and $i = N$ corresponds to $|\tilde{\mathbf{p}}_N| = e^{7/2} T_{\chi\text{PT}}$. Note that because of entropy conservation — which holds except for when the axion dominates the energy density of the universe before decaying — each fixed comoving momentum equals the ratio of the physical momentum to the temperature, $|\mathbf{p}|/T$. We have verified the convergence of our results by checking that N_{eff} changes by less than 1% when using larger N. In addition, our results for N_{eff} for just the Standard Model cosmology, or equivalently, when the axion decays far before neutrino decoupling, is 3.040. This value slightly differs from the true Standard Model value of $N_{\text{eff}}^{\text{SM}} = 3.044$ [51, 85, 86] by $\sim 0.2\%$ because we do not include effects from QED corrections or neutrino oscillations.

The dynamical timescale ($\sim 1/H$, where H is Hubble) involved in the cosmological evolution of the Boltzmann equation spans many orders of magnitude from the end of the QCD phase transition to past neutrino decoupling. Hence, we solve the system of Boltzmann equations in terms of the logarithmic timescale $y = \ln(t/t_{\chi\text{PT}})$, where $t_{\chi\text{PT}} = 1/2H(T_{\chi\text{PT}})$ is the starting time of the Boltzmann code.

Last, we determine the extra QCD contributions to the energy density ($\rho_{\delta_{\text{QCD}}}$) and pressure ($P_{\delta_{\text{QCD}}}$) arising from heavy mesons and from ideal gas law deviations using the calculations of [58], which tabulated $g_*(T)$ and $g_{*S}(T)$ for the Standard Model across the QCD phase transition. The top left panel of figure 18 shows g_* as a function of temperature T. The orange contour shows the value of g_* assuming an ideal gas comprised of photons,

JHEP04(2024)130

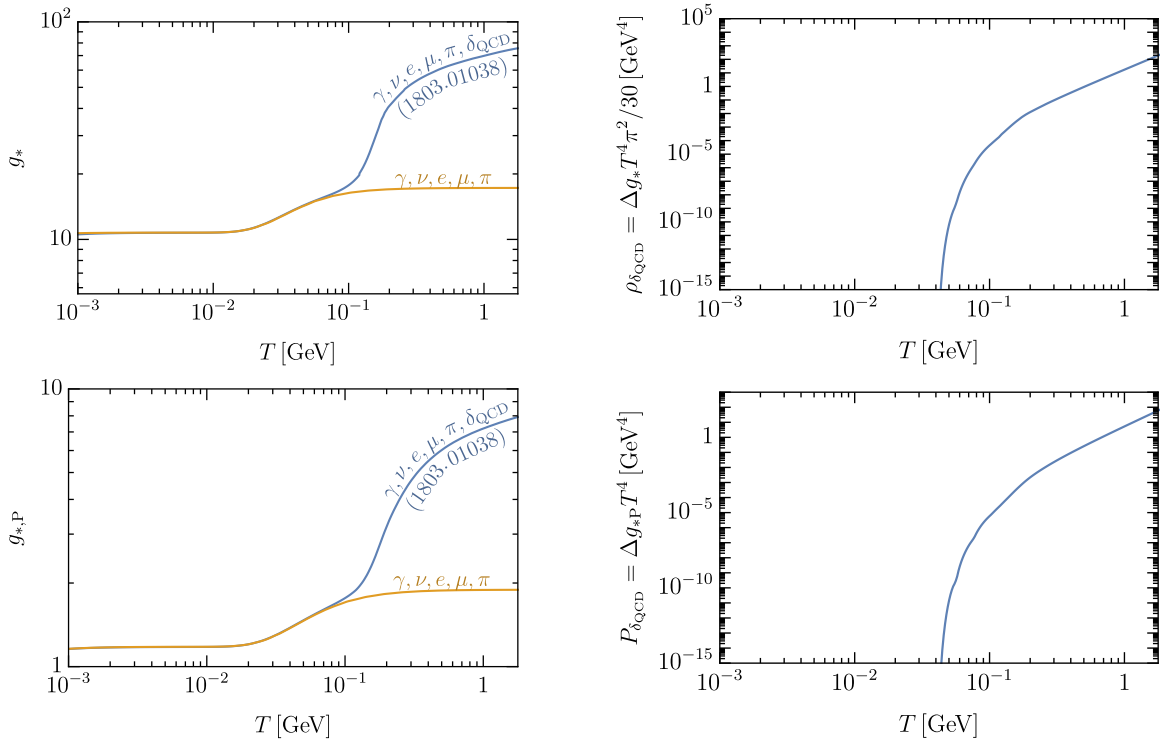

Figure 18. Top left: the orange contour shows g_* as a function of temperature assuming an ideal gas of photons, neutrinos, electrons, muons, and pions, while the blue contour shows g_* for the Standard Model including heavy mesons and deviations from the ideal gas law [58]. Top right: $\rho_{\delta \rm QCD}$ as a function of temperature, extracted from the difference in the blue and orange g_* contours on the top left panel. Bottom panels: same as top panels but for $g_{*P} \equiv P/T^4$.

neutrinos, electrons, muons, and pions in thermal equilibrium. The blue contour, which diverges from the orange above $T \sim 100\,\text{MeV}$, is the Standard Model value of g_* from [58], which includes contributions, $\delta_{\rm QCD}$, from heavy mesons and from ideal gas law deviations. We extract $\rho_{\delta_{\rm QCD}}$ by taking the difference between the blue and orange contours, Δg_*, and multiplying this result by $\pi^2 T^4/30$, as shown by the top right panel.

Similarly, the bottom left panel of figure 18 shows the ratio $P/T^4 = g_{*P}$ as a function of temperature T, where P is the total pressure of the relevant species. As before, the orange contour shows the value of g_{*P} assuming an ideal gas comprised of photons, neutrinos, electrons, muons, and pions in thermal equilibrium. The blue contour, which diverges from the orange above $T \sim 100\,\text{MeV}$, is the Standard Model value of g_{*P} from [58], which we infer through the relationship $g_{*P} = \frac{\pi^2}{30}(\frac{4}{3} g_{*S} - g_*)$. We extract $P_{\delta_{\rm QCD}}$ by taking the difference between the blue and orange contours, Δg_{*P}, and multiplying this result by T^4, as shown by the bottom right panel.

Open Access. This article is distributed under the terms of the Creative Commons Attribution License (CC-BY4.0), which permits any use, distribution and reproduction in any medium, provided the original author(s) and source are credited.

JHEP04(2024)130

References

[1] A.E. Nelson, *Naturally Weak CP Violation*, *Phys. Lett. B* **136** (1984) 387 [INSPIRE].

[2] S.M. Barr, *Solving the Strong CP Problem Without the Peccei-Quinn Symmetry*, *Phys. Rev. Lett.* **53** (1984) 329 [INSPIRE].

[3] M.A.B. Beg and H.-S. Tsao, *Strong P, T Noninvariances in a Superweak Theory*, *Phys. Rev. Lett.* **41** (1978) 278 [INSPIRE].

[4] R.N. Mohapatra and G. Senjanovic, *Natural Suppression of Strong p and t Noninvariance*, *Phys. Lett. B* **79** (1978) 283 [INSPIRE].

[5] K.S. Babu and R.N. Mohapatra, *A Solution to the Strong CP Problem Without an Axion*, *Phys. Rev. D* **41** (1990) 1286 [INSPIRE].

[6] R.D. Peccei and H.R. Quinn, *CP Conservation in the Presence of Instantons*, *Phys. Rev. Lett.* **38** (1977) 1440 [INSPIRE].

[7] R.D. Peccei and H.R. Quinn, *Constraints Imposed by CP Conservation in the Presence of Instantons*, *Phys. Rev. D* **16** (1977) 1791 [INSPIRE].

[8] H.M. Georgi, L.J. Hall and M.B. Wise, *Grand Unified Models With an Automatic Peccei-Quinn Symmetry*, *Nucl. Phys. B* **192** (1981) 409 [INSPIRE].

[9] D. Harlow and H. Ooguri, *Symmetries in quantum field theory and quantum gravity*, *Commun. Math. Phys.* **383** (2021) 1669 [arXiv:1810.05338] [INSPIRE].

[10] T. Banks and N. Seiberg, *Symmetries and Strings in Field Theory and Gravity*, *Phys. Rev. D* **83** (2011) 084019 [arXiv:1011.5120] [INSPIRE].

[11] R. Holman et al., *Solutions to the strong CP problem in a world with gravity*, *Phys. Lett. B* **282** (1992) 132 [hep-ph/9203206] [INSPIRE].

[12] S.M. Barr and D. Seckel, *Planck scale corrections to axion models*, *Phys. Rev. D* **46** (1992) 539 [INSPIRE].

[13] M. Kamionkowski and J. March-Russell, *Planck scale physics and the Peccei-Quinn mechanism*, *Phys. Lett. B* **282** (1992) 137 [hep-th/9202003] [INSPIRE].

[14] M. Dine, *Problems of naturalness: Some lessons from string theory*, in the proceedings of the *Conference on Topics in Quantum Gravity*, Cincinnati, U.S.A., April 03–04 (1992) [hep-th/9207045] [INSPIRE].

[15] K.-W. Choi, D.B. Kaplan and A.E. Nelson, *Is CP a gauge symmetry?*, *Nucl. Phys. B* **391** (1993) 515 [hep-ph/9205202] [INSPIRE].

[16] M. Dine, R.G. Leigh and D.A. MacIntire, *Of CP and other gauge symmetries in string theory*, *Phys. Rev. Lett.* **69** (1992) 2030 [hep-th/9205011] [INSPIRE].

[17] K. Choi and J.E. Kim, *DYNAMICAL AXION*, *Phys. Rev. D* **32** (1985) 1828 [INSPIRE].

[18] D. Cadamuro and J. Redondo, *Cosmological bounds on pseudo Nambu-Goldstone bosons*, *JCAP* **02** (2012) 032 [arXiv:1110.2895] [INSPIRE].

[19] Planck collaboration, *Planck 2018 results. VI. Cosmological parameters*, *Astron. Astrophys.* **641** (2020) A6 [*Erratum ibid.* **652** (2021) C4] [arXiv:1807.06209] [INSPIRE].

[20] CMB-S4 collaboration, *CMB-S4 Science Book, First Edition*, arXiv:1610.02743 [INSPIRE].

[21] S. Chang and K. Choi, *Hadronic axion window and the big bang nucleosynthesis*, *Phys. Lett. B* **316** (1993) 51 [hep-ph/9306216] [INSPIRE].

JHEP04(2024)130

[22] R.Z. Ferreira and A. Notari, *Observable Windows for the QCD Axion Through the Number of Relativistic Species*, *Phys. Rev. Lett.* **120** (2018) 191301 [arXiv:1801.06090] [INSPIRE].

[23] F. Arias-Aragón et al., *Cosmic Imprints of XENON1T Axions*, *JCAP* **11** (2020) 025 [arXiv:2007.06579] [INSPIRE].

[24] F. Arias-Aragón et al., *Production of Thermal Axions across the ElectroWeak Phase Transition*, *JCAP* **03** (2021) 090 [arXiv:2012.04736] [INSPIRE].

[25] R.Z. Ferreira, A. Notari and F. Rompineve, *Dine-Fischler-Srednicki-Zhitnitsky axion in the CMB*, *Phys. Rev. D* **103** (2021) 063524 [arXiv:2012.06566] [INSPIRE].

[26] F. D'Eramo, F. Hajkarim and S. Yun, *Thermal Axion Production at Low Temperatures: A Smooth Treatment of the QCD Phase Transition*, *Phys. Rev. Lett.* **128** (2022) 152001 [arXiv:2108.04259] [INSPIRE].

[27] F. D'Eramo, F. Hajkarim and S. Yun, *Thermal QCD Axions across Thresholds*, *JHEP* **10** (2021) 224 [arXiv:2108.05371] [INSPIRE].

[28] F. D'Eramo and S. Yun, *Flavor violating axions in the early Universe*, *Phys. Rev. D* **105** (2022) 075002 [arXiv:2111.12108] [INSPIRE].

[29] S. Hannestad and G. Raffelt, *Cosmological mass limits on neutrinos, axions, and other light particles*, *JCAP* **04** (2004) 008 [hep-ph/0312154] [INSPIRE].

[30] W. Giarè, E. Di Valentino, A. Melchiorri and O. Mena, *New cosmological bounds on hot relics: axions and neutrinos*, *Mon. Not. Roy. Astron. Soc.* **505** (2021) 2703 [arXiv:2011.14704] [INSPIRE].

[31] L. Caloni, M. Gerbino, M. Lattanzi and L. Visinelli, *Novel cosmological bounds on thermally-produced axion-like particles*, *JCAP* **09** (2022) 021 [arXiv:2205.01637] [INSPIRE].

[32] S. Dimopoulos, *A Solution of the Strong CP Problem in Models With Scalars*, *Phys. Lett. B* **84** (1979) 435 [INSPIRE].

[33] S.H.H. Tye, *A Superstrong Force With a Heavy Axion*, *Phys. Rev. Lett.* **47** (1981) 1035 [INSPIRE].

[34] B. Holdom and M.E. Peskin, *Raising the Axion Mass*, *Nucl. Phys. B* **208** (1982) 397 [INSPIRE].

[35] B. Holdom, *Strong QCD at High-energies and a Heavy Axion*, *Phys. Lett. B* **154** (1985) 316 [*Erratum ibid.* **156** (1985) 452] [INSPIRE].

[36] J.M. Flynn and L. Randall, *A Computation of the Small Instanton Contribution to the Axion Potential*, *Nucl. Phys. B* **293** (1987) 731 [INSPIRE].

[37] P. Agrawal and K. Howe, *Factoring the Strong CP Problem*, *JHEP* **12** (2018) 029 [arXiv:1710.04213] [INSPIRE].

[38] T. Gherghetta, V.V. Khoze, A. Pomarol and Y. Shirman, *The Axion Mass from 5D Small Instantons*, *JHEP* **03** (2020) 063 [arXiv:2001.05610] [INSPIRE].

[39] V.A. Rubakov, *Grand unification and heavy axion*, *JETP Lett.* **65** (1997) 621 [hep-ph/9703409] [INSPIRE].

[40] Z. Berezhiani, L. Gianfagna and M. Giannotti, *Strong CP problem and mirror world: The Weinberg-Wilczek axion revisited*, *Phys. Lett. B* **500** (2001) 286 [hep-ph/0009290] [INSPIRE].

[41] S. Weinberg, *A New Light Boson?*, *Phys. Rev. Lett.* **40** (1978) 223 [INSPIRE].

[42] F. Wilczek, *Problem of Strong P and T Invariance in the Presence of Instantons*, *Phys. Rev. Lett.* **40** (1978) 279 [INSPIRE].

JHEP04(2024)130

[43] H. Fukuda, K. Harigaya, M. Ibe and T.T. Yanagida, *Model of visible QCD axion*, *Phys. Rev. D* **92** (2015) 015021 [arXiv:1504.06084] [INSPIRE].

[44] A. Hook, S. Kumar, Z. Liu and R. Sundrum, *High Quality QCD Axion and the LHC*, *Phys. Rev. Lett.* **124** (2020) 221801 [arXiv:1911.12364] [INSPIRE].

[45] K.J. Kelly, S. Kumar and Z. Liu, *Heavy axion opportunities at the DUNE near detector*, *Phys. Rev. D* **103** (2021) 095002 [arXiv:2011.05995] [INSPIRE].

[46] J.E. Kim, *Weak Interaction Singlet and Strong CP Invariance*, *Phys. Rev. Lett.* **43** (1979) 103 [INSPIRE].

[47] M.A. Shifman, A.I. Vainshtein and V.I. Zakharov, *Can Confinement Ensure Natural CP Invariance of Strong Interactions?*, *Nucl. Phys. B* **166** (1980) 493 [INSPIRE].

[48] M. Millea, L. Knox and B. Fields, *New Bounds for Axions and Axion-Like Particles with keV-GeV Masses*, *Phys. Rev. D* **92** (2015) 023010 [arXiv:1501.04097] [INSPIRE].

[49] P.F. Depta, M. Hufnagel and K. Schmidt-Hoberg, *Robust cosmological constraints on axion-like particles*, *JCAP* **05** (2020) 009 [arXiv:2002.08370] [INSPIRE].

[50] D. Aloni, Y. Soreq and M. Williams, *Coupling QCD-Scale Axionlike Particles to Gluons*, *Phys. Rev. Lett.* **123** (2019) 031803 [arXiv:1811.03474] [INSPIRE].

[51] Particle Data Group collaboration, *Review of Particle Physics*, *PTEP* **2020** (2020) 083C01 [INSPIRE].

[52] A. Salvio, A. Strumia and W. Xue, *Thermal axion production*, *JCAP* **01** (2014) 011 [arXiv:1310.6982] [INSPIRE].

[53] L. Di Luzio, G. Martinelli and G. Piazza, *Breakdown of chiral perturbation theory for the axion hot dark matter bound*, *Phys. Rev. Lett.* **126** (2021) 241801 [arXiv:2101.10330] [INSPIRE].

[54] P. Graf and F.D. Steffen, *Thermal axion production in the primordial quark-gluon plasma*, *Phys. Rev. D* **83** (2011) 075011 [arXiv:1008.4528] [INSPIRE].

[55] D. Cadamuro, S. Hannestad, G. Raffelt and J. Redondo, *Cosmological bounds on sub-MeV mass axions*, *JCAP* **02** (2011) 003 [arXiv:1011.3694] [INSPIRE].

[56] H.A. Weldon, *Covariant Calculations at Finite Temperature: The Relativistic Plasma*, *Phys. Rev. D* **26** (1982) 1394 [INSPIRE].

[57] S. Hannestad, A. Mirizzi and G. Raffelt, *New cosmological mass limit on thermal relic axions*, *JCAP* **07** (2005) 002 [hep-ph/0504059] [INSPIRE].

[58] K. Saikawa and S. Shirai, *Primordial gravitational waves, precisely: The role of thermodynamics in the Standard Model*, *JCAP* **05** (2018) 035 [arXiv:1803.01038] [INSPIRE].

[59] *The Numerical Method of Lines*, https://reference.wolfram.com/language/tutorial/NDSolveMethodOfLines.html.

[60] F. Ertas and F. Kahlhoefer, *On the interplay between astrophysical and laboratory probes of MeV-scale axion-like particles*, *JHEP* **07** (2020) 050 [arXiv:2004.01193] [INSPIRE].

[61] B. Döbrich et al., *ALPtraum: ALP production in proton beam dump experiments*, *JHEP* **02** (2016) 018 [arXiv:1512.03069] [INSPIRE].

[62] M.J. Dolan et al., *Revised constraints and Belle II sensitivity for visible and invisible axion-like particles*, *JHEP* **12** (2017) 094 [*Erratum ibid.* **03** (2021) 190] [arXiv:1709.00009] [INSPIRE].

[63] NA64 collaboration, *Search for Axionlike and Scalar Particles with the NA64 Experiment*, *Phys. Rev. Lett.* **125** (2020) 081801 [arXiv:2005.02710] [INSPIRE].

JHEP04(2024)130

[64] FASER collaboration, *FASER's physics reach for long-lived particles*, *Phys. Rev. D* **99** (2019) 095011 [arXiv:1811.12522] [INSPIRE].

[65] S. Gori, G. Perez and K. Tobioka, *KOTO vs. NA62 Dark Scalar Searches*, *JHEP* **08** (2020) 110 [arXiv:2005.05170] [INSPIRE].

[66] A. Mariotti, D. Redigolo, F. Sala and K. Tobioka, *New LHC bound on low-mass diphoton resonances*, *Phys. Lett. B* **783** (2018) 13 [arXiv:1710.01743] [INSPIRE].

[67] S. Chakraborty et al., *Heavy QCD axion in b→s transition: Enhanced limits and projections*, *Phys. Rev. D* **104** (2021) 055036 [*Erratum ibid.* **108** (2023) 039903] [arXiv:2102.04474] [INSPIRE].

[68] E. Bertholet et al., *Heavy QCD axion at Belle II: Displaced and prompt signals*, *Phys. Rev. D* **105** (2022) L071701 [arXiv:2108.10331] [INSPIRE].

[69] D. Dunsky, L.J. Hall and K. Harigaya, *Dark Matter, Dark Radiation and Gravitational Waves from Mirror Higgs Parity*, *JHEP* **02** (2020) 078 [arXiv:1908.02756] [INSPIRE].

[70] D. Dunsky, L.J. Hall and K. Harigaya, *CHAMP Cosmic Rays*, *JCAP* **07** (2019) 015 [arXiv:1812.11116] [INSPIRE].

[71] W.L. Xu, J.B. Muñoz and C. Dvorkin, *Cosmological constraints on light but massive relics*, *Phys. Rev. D* **105** (2022) 095029 [arXiv:2107.09664] [INSPIRE].

[72] C. O'Hare, *cajohare/axionlimits: Axionlimits*, DOI:10.5281/zenodo.3932430.

[73] J. Preskill, M.B. Wise and F. Wilczek, *Cosmology of the Invisible Axion*, *Phys. Lett. B* **120** (1983) 127 [INSPIRE].

[74] L.F. Abbott and P. Sikivie, *A Cosmological Bound on the Invisible Axion*, *Phys. Lett. B* **120** (1983) 133 [INSPIRE].

[75] M. Dine and W. Fischler, *The Not So Harmless Axion*, *Phys. Lett. B* **120** (1983) 137 [INSPIRE].

[76] J.H. Chang, R. Essig and S.D. McDermott, *Supernova 1987A Constraints on Sub-GeV Dark Sectors, Millicharged Particles, the QCD Axion, and an Axion-like Particle*, *JHEP* **09** (2018) 051 [arXiv:1803.00993] [INSPIRE].

[77] A. Ayala et al., *Revisiting the bound on axion-photon coupling from Globular Clusters*, *Phys. Rev. Lett.* **113** (2014) 191302 [arXiv:1406.6053] [INSPIRE].

[78] CAST collaboration, *An improved limit on the axion-photon coupling from the CAST experiment*, *JCAP* **04** (2007) 010 [hep-ex/0702006] [INSPIRE].

[79] CAST collaboration, *New CAST Limit on the Axion-Photon Interaction*, *Nature Phys.* **13** (2017) 584 [arXiv:1705.02290] [INSPIRE].

[80] N. Vinyoles et al., *New axion and hidden photon constraints from a solar data global fit*, *JCAP* **10** (2015) 015 [arXiv:1501.01639] [INSPIRE].

[81] M. Kawasaki, K. Kohri and N. Sugiyama, *Cosmological constraints on late time entropy production*, *Phys. Rev. Lett.* **82** (1999) 4168 [astro-ph/9811437] [INSPIRE].

[82] M. Kawasaki, K. Kohri and N. Sugiyama, *MeV scale reheating temperature and thermalization of neutrino background*, *Phys. Rev. D* **62** (2000) 023506 [astro-ph/0002127] [INSPIRE].

[83] T. Hasegawa et al., *MeV-scale reheating temperature and thermalization of oscillating neutrinos by radiative and hadronic decays of massive particles*, *JCAP* **12** (2019) 012 [arXiv:1908.10189] [INSPIRE].

JHEP04(2024)130

[84] S. Hannestad and J. Madsen, *Neutrino decoupling in the early universe*, *Phys. Rev. D* **52** (1995) 1764 [astro-ph/9506015] [INSPIRE].

[85] J.J. Bennett et al., *Towards a precision calculation of $N_{\rm eff}$ in the Standard Model II: Neutrino decoupling in the presence of flavour oscillations and finite-temperature QED*, *JCAP* **04** (2021) 073 [arXiv:2012.02726] [INSPIRE].

[86] J. Froustey, C. Pitrou and M.C. Volpe, *Neutrino decoupling including flavour oscillations and primordial nucleosynthesis*, *JCAP* **12** (2020) 015 [arXiv:2008.01074] [INSPIRE].

JHEP04(2024)130